

# SEARCHING FOR LOW SURFACE-BRIGHTNESS GALAXIES IN THE HUBBLE ULTRA DEEP FIELD: IMPLICATIONS FOR THE STAR FORMATION EFFICIENCY IN NEUTRAL GAS AT $z \sim 3$ <sup>1</sup>

Arthur M. Wolfe

Department of Physics, and Center for Astrophysics and Space Sciences;  
University of California, San Diego;  
9500 Gilman Dr.  
La Jolla, CA 92093-0424  
**awolfe@ucsd.edu**

and

Hsiao-Wen Chen

Department of Astronomy & Astrophysics,  
University of Chicago;  
Chicago, IL 60637  
**hchen@oddjob.uchicago.edu**

## ABSTRACT

The Kennicutt–Schmidt law relates the face-on star formation rate (SFR) per unit area with the face-on gaseous column density in nearby galaxies. Applying this relation to damped Ly $\alpha$  absorption systems (DLAs) of neutral hydrogen column density  $N > 1.6 \times 10^{21} \text{ cm}^{-2}$  leads to an estimate that three percent of the sky should be covered with extended sources brighter than  $\mu_V \approx 28.4 \text{ mag arcsec}^{-2}$ , if DLAs at redshift  $z=[2.5,3.5]$  undergo *in situ* star formation. We test this hypothesis by searching the Hubble Ultra Deep Field (UDF) F606W image for low surface-brightness features of angular sizes, ranging between  $\theta_{\text{dla}}=0.25''$  and  $4.0''$ . At  $z = 2.5 - 3.5$ , the observed F606W fluxes correspond to roughly rest-frame  $1500 \text{ \AA}$  and the angular sizes correspond to predicted disk diameters of  $d_{\text{dla}} = 2 - 31 \text{ kpc}$ . After convolving the F606W image with smoothing kernels of angular diameters  $\theta_{\text{kern}}=\theta_{\text{dla}}$ , we find the number of detected objects to decrease rapidly to zero at  $\theta_{\text{kern}}>1''$ . Our search yields upper limits on the comoving SFR densities that are between factors of 30 and 100 lower than predictions, suggesting a reduction by more than a factor of 10 in star formation efficiency at  $z \sim 3$ . We consider several mechanisms that could reduce star formation efficiency at high redshift. We find that the cosmological increase with redshift of the critical surface density for the Toomre instability may be sufficient to suppress star formation to the levels implied by

---

<sup>1</sup>Based on observations obtained with the NASA/ESA *Hubble Space Telescope*. *HST* is operated by the Association of Universities for Research in Astronomy (AURA), Inc., under NASA contract NASS5-26555.

the UDF observations. However, the uncertainties are such that Toomre instabilities may still exist. In that case star formation at column densities less than  $10^{22} \text{ cm}^{-2}$  may be suppressed by the low molecular content of the DLA gas. The upper limits on *in situ* star formation reduce the predicted metallicities at  $z \sim 3$  to be significantly lower than observed, and reduce the heat input in the gas to be substantially lower than the inferred cooling rates. In contrast, the radiative output from compact Lyman Break Galaxies (LBGs) with  $R < 27$  is sufficient to balance the comoving cooling rate. This leads us to posit that a significant fraction of the DLA population are hosts to more compact regions of active star formation, which may be the sources of metal enrichment for these DLAs. Such regions are likely to be LBGs.

*Subject headings:* cosmology—galaxies: evolution—galaxies: quasars—absorption lines

## 1. INTRODUCTION

A principal goal of galaxy formation theory is to understand how stars form from gas. This condensation process is fundamental for determining the star-formation history of a galaxy, the spatial distributions of its stellar populations, and its chemical evolution. Yet it is still not understood. On small scales, the physical processes are complex and difficult to calculate (e.g. Shu et al. 1987; Krumholz & McKee 2005), while on cosmological scales, realistic simulations of star formation are in addition constrained by limits on numerical resolution (e.g. Cen et al. 2003; Nagamine et al. 2004a, 2004b). On the other hand considerable progress has been made in the observational sector. Recent multi-color imaging and spectroscopic surveys have succeeded in tracing starburst galaxies out to redshifts as large as six (Giavalisco et al. 2004; Bouwens et al. 2004). The majority of galaxies found in this way are the Lyman Break Galaxies (i.e. LBGs; e.g. Steidel et al. 2003). These are compact (half-light *diameters*  $\sim 4$  kpc) star-forming galaxies with mean star formation rates  $\text{SFR} \sim 40 M_{\odot} \text{ yr}^{-1}$ , after extinction corrections are applied (Shapley et al. 2003). The LBGs contribute a SFR per unit comoving volume  $\dot{\rho}_{*}(z)$  (Steidel et al. 1999; Giavalisco et al. 2004) that in the redshift interval  $z = [6, 2]$  would consume a mass per unit comoving volume of cold neutral gas equivalent to about 10 % of the mass content of visible stars in modern galaxies, i.e.,  $0.1\Omega_{*}(z = 0)$ . As a result, reservoirs of neutral gas at  $z \geq 2$  may be required to fuel these star-forming objects.

The purpose of this paper is to search for star formation in spatially extended regions that serve as such neutral-gas reservoirs. We focus on the damped  $\text{Ly}\alpha$  systems (hereafter DLAs), the population of quasar absorption systems with  $N \geq 2 \times 10^{20} \text{ cm}^{-2}$ , where  $N$  denotes observed H I column density (for a review see Wolfe, Gawiser, & Prochaska 2005 [hereafter WGP05]). At  $z \sim 3$  this column-density threshold guarantees gas neutrality in most cases, which distinguishes DLAs from the  $\text{Ly}\alpha$  forest and all other classes of absorption systems in which  $N < 2 \times 10^{20} \text{ cm}^{-2}$  and the gas is more than 50 % ionized. The neutrality of the gas takes on added significance when it is realized that DLAs (1) dominate the neutral-gas content of the Universe at  $z = [0, 5]$  and (2) at

$z \approx 3.5$  contain sufficient gas to account for  $0.5\Omega_*(z=0)$ . Furthermore surveys for DLAs reveal a large area-covering factor for neutral gas with  $N \geq 2 \times 10^{20} \text{ cm}^{-2}$  (Wolfe et al. 1995; Prochaska, Herbert-Fort, & Wolfe 2005 [PHW05]). In the redshift interval  $z=[2.5,3.5]$ , a redshift range in which the SFR history of galaxies is well determined, DLAs cover one third of the sky, which leads to a striking conclusion: the sky should be “lit up” with star formation. Specifically, a subset of DLAs with  $N > 1.6 \times 10^{21} \text{ cm}^{-2}$  should cover three percent of the sky and have surface brightnesses brighter than  $28.4 \text{ mag arcsec}^{-2}$  (see below). This follows if one presumes the Kennicutt–Schmidt law (Schmidt 1959; Kennicutt 1998a,b) holds at high redshifts. In that case star formation occurs in the presence of cold atomic and/or molecular gas with a SFR per unit area projected perpendicular to the disk given by

$$(\dot{\psi}_*)_{\perp} = \begin{cases} 0 ; N_{\perp} < N_{\perp}^{crit} \\ K \times [N_{\perp}/N_c]^{\beta} ; N_{\perp} \geq N_{\perp}^{crit}, \end{cases} \quad (1)$$

where  $N_{\perp}$  is the H I column density perpendicular to the disk. In nearby galaxies,  $K=K_{Kenn}=(2.5 \pm 0.5) \times 10^{-4} \text{ M}_{\odot} \text{ yr}^{-1} \text{ kpc}^{-2}$ ,  $\beta=1.4 \pm 0.15$ , and the scale factor  $N_c=1.25 \times 10^{20} \text{ cm}^{-2}$  (Kennicutt 1998a,b). The threshold column density  $N_{\perp}^{crit}$  is observed to range between  $5 \times 10^{20} \text{ cm}^{-2}$  and  $2 \times 10^{21} \text{ cm}^{-2}$  (Kennicutt 1998b) and is usually associated with the threshold condition for the Toomre instability. We ignore the molecular component of the gas owing to the very low  $\text{H}_2$  area covering factor of DLAs (e.g. Ledoux et al. 2003).

In this paper, we test the hypothesis that star formation proceeds throughout the absorbing gas at the projected rates given by Eq. 1. That is, we consider whether star formation at high  $z$  occurs in sites other than compact LBGs. In § 2 we apply Eq. 1 to high- $z$  DLAs and compute their expected surface brightnesses. We compute for the first time the SFR per unit comoving volume for DLAs modeled as randomly oriented disks. We then calculate the number of DLAs expected to occupy the Hubble Ultra Deep Field (UDF; S. V. W. Beckwith et al. 2004, in preparation). In § 3 we describe a search in the UDF for extended regions with low surface brightnesses. We use a matched kernel technique optimized for detecting faint emission from extended objects and discuss the results of our search in § 4. In § 5 we describe the implications of these results. A summary and concluding remarks are given in § 6.

Throughout this paper we adopt a cosmology with  $(\Omega_M, \Omega_{\Lambda}, h)=(0.3, 0.7, 0.7)$  (Spergel et al. 2003). We adopt the AB magnitude system and refer to magnitudes and surface brightnesses deduced from the F606W image with the ACS camera on HST as follows:  $V \equiv AB(\text{F606W})$  and  $\mu_V \equiv \mu_{\text{F606W}}$ .

## 2. THEORETICAL FRAMEWORK

Before describing the observational results and analysis we discuss observational properties predicted for DLAs relevant for detecting them in emission.

## 2.1. Comoving SFR Densities Predicted by the Kennicutt–Schmidt Law

In order to estimate the surface brightnesses of DLAs with projected SFRs predicted by the Kennicutt–Schmidt law, we assume they are disks inclined to the plane of the sky by inclination angles  $i$ . In that case the observed intensity at frequency  $\nu_0$  is given by

$$I_{\nu_0}(i) = \frac{(\Sigma_\nu)_\perp}{4\pi(1+z)^3\cos(i)} \quad , \quad (2)$$

where  $(\Sigma_\nu)_\perp$  is the luminosity per unit frequency interval per unit area projected perpendicular to the plane of the disk and  $\nu = (1+z)\nu_0$ : owing to the low dust-to-gas ratios of most DLAs (Pettini 2004), we ignore the effects of extinction. In the case of FUV radiation (with  $\lambda \approx 1500 \text{ \AA}$ ),  $(\Sigma_\nu)_\perp = C (\dot{\psi}_*)_\perp$  where  $C = 8 \times 10^{27} \text{ ergs s}^{-1} \text{ Hz}^{-1} (\text{M}_\odot \text{ yr}^{-1})^{-1} / (3.08 \times 10^{21} \text{ cm/kpc})^2 = 8.4 \times 10^{-16} \text{ ergs cm}^{-2} \text{ s}^{-1} \text{ Hz}^{-1} (\text{M}_\odot \text{ yr}^{-1} \text{ kpc}^{-2})^{-1}$ , where the calibration is insensitive to wavelength in the FUV portion of the spectrum (Madau, Pozzetti, & Dickinson 1998). Because  $N_\perp = \cos(i)N$ , we find that, for a fixed observed column density,  $I_{\nu_0}(i)$  averaged over  $0^\circ \leq i \leq 90^\circ$  is given by

$$\langle I_{\nu_0} \rangle = \frac{C\dot{\psi}_*}{4\pi(1+z)^3\beta} \quad , \quad \dot{\psi}_* \equiv K(N/N_c)^\beta \quad . \quad (3)$$

Note that  $\dot{\psi}_*$  is *not* the average SFR per unit area projected along the line of sight,  $\langle (\dot{\psi}_*)_\perp / \cos(i) \rangle$ . Rather it is an effective projected SFR relating the observed column density,  $N$ , to the surface brightness of the DLA. As an example, consider a DLA with  $N = 1.6 \times 10^{21} \text{ cm}^{-2}$ , which is about twice the mean value of  $N$  for the statistical sample of over 625 DLAs (PHW05). From Eq. 3 we find  $\dot{\psi}_* = 8.9 \times 10^{-3} \text{ M}_\odot \text{ yr}^{-1} \text{ kpc}^{-2}$  (about twice the local rate in the Galaxy). At  $z = 3$  this corresponds to an  $AB$  surface brightness in the  $V$  band,  $\mu_V = 28.4 \text{ mag arcsec}^{-2}$ . Here we assumed the values for  $K$ ,  $\beta$ , and  $N_c$  cited above (Kennicutt 1998a,b). While objects this faint are beyond the sensitivity of the Hubble Deep Field (HDF) and the GOODS survey, they are within the sensitivity of images acquired by the UDF (Bouwens et al. 2004).

We next compute the comoving SFR density  $\dot{\rho}_*(z)$  predicted by the Kennicutt–Schmidt law in order to compare it with the empirical values determined from the UDF (see § 3). The calculation was originally carried out by Lanzetta et al. (2002: see also Hopkins et al. 2005). Here for the first time we account for inclination effects that must be present if, as we assume, DLAs are disk-like structures or any type of gaseous configurations with preferred planes of symmetry, such as those predicted in high-resolution numerical simulations (e.g. Razoumov et al. 2005; Kravtsov 2003). For disks with inclination angles between  $i$  and  $i + di$  the comoving SFR density due to the intrinsic differential area  $dA_\perp$  of the disk is given by

$$d^2\dot{\rho}_* = n_{co}dA_\perp \cos(i) \times [(\dot{\psi}_*)_\perp / \cos(i)] \times \sin(i)di \quad , \quad (4)$$

where  $n_{co}$  is the comoving density of disks. Noting that the intrinsic column-density distribution of the disk is defined by the relation

$$g(N_{\perp}, X)dN_{\perp} \equiv (c/H_0)n_{co}(X)dA_{\perp} \quad , \quad (5)$$

and  $\cos(i)=N_{\perp}/N$  and  $\sin(i)di=(N_{\perp}/N^2)dN$  we find that

$$\dot{\rho}_*(\geq N, X) = (H_0/c) \int_N^{N_{max}} dN K(N/N_c)^{\beta} \int_{N_{min}}^{\min(N_0, N)} dN_{\perp} g(N_{\perp}, X) (N_{\perp}^2/N^3) (N_{\perp}/N)^{\beta-1} \quad , \quad (6)$$

where  $g(N_{\perp}, X)$  and the observed column-density distribution function  $f(N, X)$  are related by

$$f(N, X) = \int_{N_{min}}^{\min(N_0, N)} dN_{\perp} g(N_{\perp}, X) (N_{\perp}^2/N^3) \quad (7)$$

(Fall & Pei 1993; Wolfe et al. 1995) and  $X(z)$  is the absorption distance (Bahcall & Peebles 1969). In deriving these equations we implicitly assumed  $N_{\perp}$  to be a monotonically decreasing function of radius with a maximum value of  $N_0$ . Note, in the spherically symmetric limit the  $(N_{\perp}/N)^{\beta-1}$  term in Eq. 6 would be replaced by 1 and consequently the expression for  $\dot{\rho}_*(\geq N, X)$  would be the same as the Lanzetta et al. (2002) result (see also Hopkins et al. 2005).

Equations 6 and 7 show that one must obtain  $g(N_{\perp}, X)$  from  $f(N, X)$  to compute  $\dot{\rho}_*(\geq N, X)$ . The double power-law fit to the SDSS data resulted in  $f(N, X) = k_3(N/N_d)^{\alpha}$  where  $k_3 = (1.48 \pm 0.07) \times 10^{-24} \text{ cm}^2$ ,  $\alpha = \alpha_3 = -2.00 \pm 0.06$  for  $N \leq N_d$  and  $\alpha = \alpha_4 = -6.00_{-3.93}^{+4.06}$  at  $N > N_d$ , where  $N_d = (3.16_{-0.28}^{+0.47}) \times 10^{21} \text{ cm}^{-2}$  (PHW05). It is natural to equate  $N_d$  with  $N_0$  in which case Eq. 7 shows that projection effects alone result in  $\alpha_4 = -3.0$ . This solution is clearly consistent with the data, given the large uncertainties in  $\alpha_4$  (note,  $\dot{\rho}_*[\geq N, X]$  is independent of  $\alpha_4$ ). As a result this fit leads to  $g(N_{\perp}, X) = k_3(N_{\perp}/N_0)^{-2}$  at  $N_{\perp} \leq N_0$  and  $g(N_{\perp}, X) = 0$  for  $N_{\perp} > N_0$ . One could envisage an alternative solution in which  $N_0 \sim 10^{22} \text{ cm}^{-2}$  and in which  $d \log g(N_{\perp}, X) / d \log N_{\perp}$  decreases below  $-3.0$  as  $N_{\perp}$  increases toward  $N_0$ . This is observed locally and is presumably due to the conversion of H I into H<sub>2</sub> at large column densities (Zwaan et al. 2006). However, the molecular fraction does not increase with  $N$  in DLAs (Ledoux et al. 2003), which is likely due to low dust content. Since the gamma distribution fit,  $f(N, X) \propto (N/N_{\gamma})^{\alpha_2} \exp(-N/N_{\gamma})$  (PHW05), leads to negative  $g(N_{\perp}, X)$  for  $N_{\perp} > (3 + \alpha_2)N_{\gamma}$ , we conclude that our double power-law fit to  $f(N, X)$ , with  $\alpha_4 = -3.0$ , is the most plausible solution for DLAs, provided they are disk-like structures, and we adopt it here and in what follows.

The resulting cumulative comoving SFR density is depicted by the blue curve in Fig. 1. We plot  $\dot{\rho}_*(\geq \dot{\psi}_*, X)$  for the range in  $\dot{\psi}_*$  corresponding to  $N = [N_{min}, N_{max}]$ , where here and unless otherwise noted,  $N_{min} = 2 \times 10^{20} \text{ cm}^{-2}$  and  $N_{max} = 10^{22} \text{ cm}^{-2}$ . By adopting a value for  $N_{min}$  that is

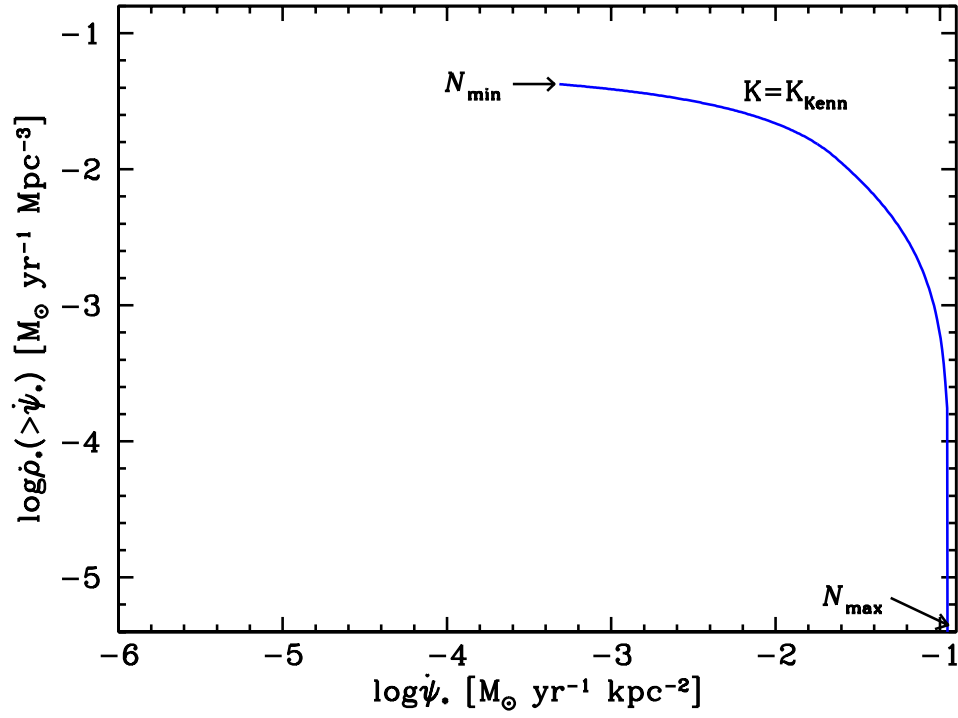


Fig. 1.— Cumulative comoving SFR density versus  $\dot{\psi}_*$ . Curve is  $\rho_*(\geq \dot{\psi}_*)$  predicted for Kennicutt-Schmidt law with  $K=K_{\text{Kenn}}$ . The range of  $\dot{\psi}_*$  corresponds to  $N=[2 \times 10^{20}, 1 \times 10^{22}]$ .

lower than the range of threshold column densities  $N_{\perp}^{crit}$  observed for nearby galaxies (Kennicutt 1998b), we overestimate  $\dot{\rho}_*(\geq N_{min})$ . However, the upper limits on  $\dot{\rho}_*$  estimated in § 3.3 are valid only for  $N$  higher than the local values of  $N_{\perp}^{crit}$ , and as a result comparison between theory and observation occurs at column densities where the Kennicutt-Schmidt law is well established. We also assume  $z=3$  and use Eq. 3 and the Kennicutt parameters to convert  $N$  to  $\dot{\psi}_*$ . In agreement with Hopkins et al. (2005) we find that  $\dot{\rho}_*$  inferred for DLAs is predicted to be somewhat lower than deduced for LBGs (Steidel et al. 1999; Giavalisco et al. 2004), or for DLAs from the C II\* technique (Wolfe et al. 2003a [hereafter WGP03]).

## 2.2. Expected Number of DLAs in the UDF

How many DLAs are expected to populate the UDF? The answer depends on three factors: (1) the column-density distribution function  $f(N, X)$ , (2) the redshift search interval  $z = [z_{low}, z_{high}]$ , and (3) the linear sizes of the DLAs. Suppose all DLAs were equal in size. Because angular diameter is an insensitive function of  $z$  at  $z > 1.2$ , we assume that all DLAs in the search volume have identical angular diameters,  $\theta_{DLA}$ . In that case the number of DLAs with column-densities greater than  $N$  is given by

$$\mathcal{N}(\geq N) = \left( \frac{\omega_{UDF}}{\pi\theta_{DLA}^2/4} \right) \int_{X(z_{low})}^{X(z_{high})} dX \int_N^{N_{max}} dN' f(N', X) \quad , \quad (8)$$

where  $\omega_{UDF}$  is the solid angle subtended by the UDF. The results shown in Fig. 2 were obtained assuming  $\omega_{UDF}=10$  arcmin<sup>2</sup>,  $z_{low}=2.5$ , and  $z_{high}=3.5$ . The four curves were computed for  $\theta_{DLA}=0.5''$ ,  $1''$ ,  $2''$ , and  $4''$ , which correspond to linear diameters of 4, 8, 15, and 31 kpc at  $z=3$  that span the range of sizes predicted for DLAs, which can reach diameters as low as 2 kpc (e.g. Haehnelt et al. 1998; Nagamine et al. 2005; Razoumov et al. 2005; Prochaska & Wolfe 1997). To evaluate the integral in Eq. 8 we combined the redshift evolution of  $d\mathcal{N}/dX$  with the  $N$ -dependence of  $f(N, X)$  determined from the full sample of DLAs found in the SDSS survey (PHW05). The figure shows the UDF should be populated by large numbers of DLAs. In our example of  $N > 1.6 \times 10^{21}$  cm<sup>-2</sup> we find that over 100 DLAs would be present with  $\mu_V < 28.4$  mag arcsec<sup>-2</sup> if  $\theta_{DLA} = 4''$ . Of course, not all DLAs will have the same size, and most should have  $\theta_{DLA} < 4''$ , which results in an increase in  $\mathcal{N}$ . The point is that the UDF should contain hundreds to tens of thousands of high column-density DLAs which according to Eq. 3 should be detectable. By comparison, were the LBG luminosity function (Adelberger & Steidel 2000) extrapolated to an approximate UDF point-source limit of  $V=30.5$ , the UDF would be populated with 1800 LBGs in the redshift interval  $z=[2.5,3.5]$ .

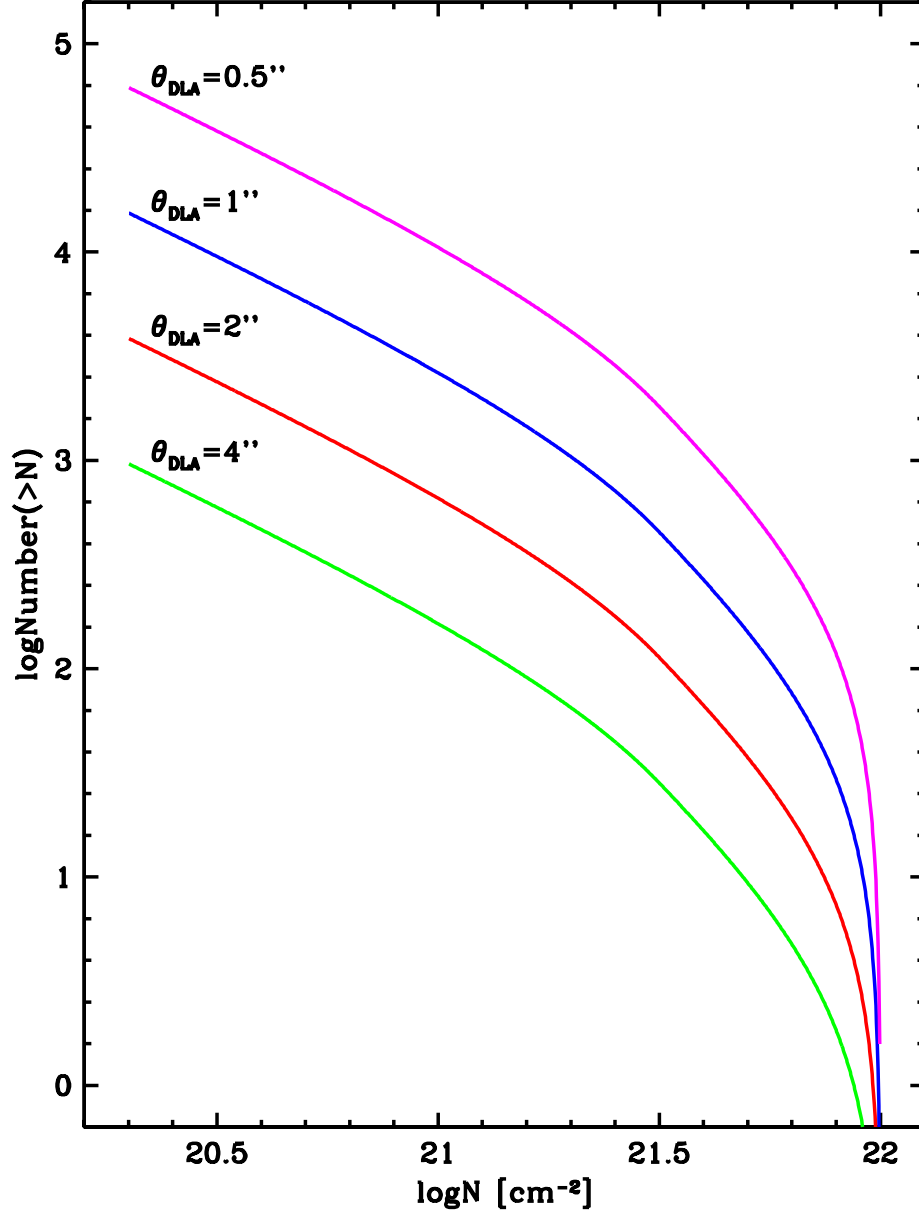


Fig. 2.— Plot showing number of DLAs with column densities exceeding  $N$  predicted to populate the UDF in the redshift interval  $z=[2.5,3.5]$ . Magenta, blue, red, and green curves are for DLAs with  $\theta_{\text{DLA}} = 0.5''$ ,  $1''$ ,  $2''$ , and  $4''$ .



### 3. ANALYSIS

We now describe the results of our search for emission from DLAs.

#### 3.1. Object Detection

To determine  $\dot{\rho}_*(\geq\dot{\psi}_*)$  (here and in what follows we let  $\dot{\rho}_*(\geq\dot{\psi}_*)\equiv\dot{\rho}_*[\geq\dot{\psi}_*,X(z=3)]$ ) empirically, we searched for extended, low surface-brightness emission in the UDF. The search was performed with images acquired with the F606W filter. The wavelength centroid of the F606W filter approximately matches the rest-frame FUV wavelength of 1500 Å for the redshift search interval  $z=[2.5,3.5]$ . This is the standard rest-frame wavelength for which the LBG luminosity function and comoving SFR densities have been determined (Steidel et al. 1999; Adelberger & Steidel 2000). Furthermore, this redshift interval contains the largest sample of known LBGs, which we shall use for comparison with our results, and the F606W image is the most sensitive one obtained in the UDF. Because the UDF does not have the  $U$ -band sensitivity required for this project and the Lyman limit discontinuities of  $z \sim 3$  objects occur further blueward of the blue filter response, photometric redshifts for objects in this redshift range are subject to catastrophic errors. We therefore apply the data only for determining *upper limits* on  $\dot{\rho}_*(\geq\dot{\psi}_*)$  by assuming that all objects lie in this redshift range.

We performed object detection in the drizzle-combined F606W image using SExtractor (Bertin & Arnouts 1996). The object detection criteria are set according to the following steps. First, we require the presence of flux over a minimum, contiguous area comparable to the size of an adopted kernel. Next, we adjusted the detection threshold to the lowest value where zero detections are found in the negative image. This procedure was first performed in the original F606W image with a smoothing kernel matching the PSF of the image. Specifically, we let the FWHM of the kernel  $\theta_{\text{kern}}=\theta_{\text{PSF}}=0.09''$ , in order to identify all the high surface brightness (HSB) objects; i.e., objects with  $\mu_V < 26$  mag arcsec<sup>-2</sup>. We then masked out all these known objects in the image by setting the associated pixels to the median sky value, in order to produce a masked-F606W image. To search for extended low surface brightness objects, we smoothed the masked-F606W image using circular Gaussian kernels with  $\theta_{\text{kern}}=\theta_{\text{dla}}$  where  $\theta_{\text{dla}}$  is the FWHM of the DLA image and let the aperture diameter equal  $\theta_{\text{kern}}$ . The advantage of smoothing is that in the limit of random noise the SNR of the surface brightness of the smoothed image is enhanced relative to the unsmoothed image by the factor  $\theta_{\text{kern}}/\theta_{\text{PSF}}$  (e.g. Gonzalez et al. 2001; Irwin et al. 1985). We emphasize that removing HSB objects detected in the unsmoothed image from all subsequent searches allows us to search for extended low surface-brightness features closer to these HSB objects in smoothed images. Consequently we are testing the hypothesis that emission from DLAs arises only from star formation in the gas detected in absorption, since the Kennicutt-Schmidt law predicts  $\mu_V$  to be

fainter than 26 mag arcsec<sup>-2</sup> for  $N=[N_{\min}, N_{\max}]$  and  $z = [2.5, 3.5]$ .<sup>2</sup>

At  $z > 2$  most HSB objects are LBGs. While the brighter,  $V < 25$ , LBGs have half-light radii,  $r_{hl} \approx 2$  kpc (Giavalisco et al. 1996), recent studies with the UDF indicate  $r_{hl}$  is smaller for fainter objects and that  $r_{hl}$  decreases with increasing redshift. Specifically Bouwens et al. (2004) find that the mean half-light radius,  $\langle r_{hl} \rangle = 0.9$  kpc for their sample of intermediate magnitude,  $z_{850, AB} < 27.5$ , objects. We shall assume a conservative upper limit  $\langle r_{hl} \rangle < 1.5$  kpc for LBGs in the UDF with  $V < 30$ . The light profiles of LBGs are well fitted with exponentials. Since exponentials have FWHM linear diameters equal to  $2r_{hl}/2.5$ , the expected FWHM angular diameters for most LBGs in our sample,  $\theta_{LBG} < 0.13''$ . By contrast the angular diameters predicted for the light-emitting regions of DLAs are systematically larger. Although the observational evidence for redshifts exceeding 1.9 suggests  $2.0 \text{ kpc} < d_{\text{dla}} < 15 \text{ kpc}$  (where  $d_{\text{dla}}$  is the FWHM linear diameter), the data sample contains only three objects (WGP05). On the other hand, theoretical arguments suggest DLAs are larger than LBGs. While the predicted sizes of DLAs are smallest for CDM models, most of the predictions for  $z \sim 3$  indicate  $d_{\text{dla}} > 1.9$  kpc. Comparison with the numerical simulations of Nagamine et al. (2006) shows that 70 % is a conservative lower limit for the fraction of  $z=3$  DLAs with  $d_{\text{dla}} > 1.9$  kpc. Similarly, Haehnelt et al. (2000) predict at least 80 % of these DLAs to have  $d_{\text{dla}} > 1.9$  kpc, while the lower limit computed by Mo et al. (1998) is 95 %. Because other models (e.g. Prochaska & Wolfe 1997; Boisser et al 2003) predict even larger sizes, current ideas about DLAs suggest that the bulk of DLAs predicted in current models have linear diameters larger than 1.9 kpc, which corresponds to  $0.25''$  for the redshift interval  $z=[2.5, 3.5]$ . We shall revisit the possible connection between DLAs and HSB objects in § 5.2.

### 3.2. Search Results

Using the  $\theta_{\text{kern}}=0.09''$  smoothing kernel, we identified roughly 11,000 objects brighter than the survey limit of  $V \leq 30.5$  and with  $\langle \mu_V \rangle \leq 26.6$  mag arcsec<sup>-2</sup> in the original F606W image over the central 10 arcmin<sup>2</sup> of the UDF. Interestingly, none of the objects satisfied our search criteria for *in situ* star formation throughout the DLA gas; i.e., low surface brightness,  $\mu_V > 26$  mag arcsec<sup>-2</sup>, and angular diameter exceeding  $0.25''$ , which corresponds to the smallest linear *diameter*<sup>3</sup> predicted for a substantial fraction of model DLAs (§3.1). We considered the “tadpole galaxies” identified at  $z < 4$  in the UDF by Straughn et al. (2006) as potential candidates because they typically consist of multiple compact components distributed over an area  $\approx 0.1 \times 1$  arcsec<sup>2</sup>: we confirm the presence and properties of all 163 “tadpole galaxies” identified by Straughn et al. (2006) and measure their

---

<sup>2</sup>We chose this surface-brightness limit because at  $z = 3$  it corresponds to  $N < 8 \times 10^{21} \text{ cm}^{-2}$ , the highest column density yet measured in the SDSS DLA survey (PHW05).

<sup>3</sup>Most discussions about DLA sizes refer to impact parameter  $b$  rather than diameter  $d$ . In the simple case of randomly oriented circular disks, the median impact parameter  $b=d/2\sqrt{2}$ , which corresponds to  $b = 0.67$  kpc for  $\theta_{\text{kern}}=0.25''$ .

average  $V$  surface brightness  $\langle \mu_V \rangle = 26.6 \text{ mag arcsec}^{-2}$ . These authors detected between 50 and 60 galaxies with provisional redshifts between 2.5 and 3.5, which leads to an area covering factor  $f_A \approx 10^{-4}$ . By contrast  $f_A=0.33$  for all DLAs in this redshift interval, and  $f_A=0.13$  for DLAs with  $N \geq 5 \times 10^{20} \text{ cm}^{-2}$ , the H I column density above which the Kennicutt–Schmidt law is firmly established (Kennicutt 1998a,b). As a result the “tadpole galaxies” cannot be the sites of *in situ* star formation in most DLAs. On the other hand, the relatively high surface brightness of the compact components in these galaxies is consistent with star formation occurring in regions with  $N > 5 \times 10^{21} \text{ cm}^{-2}$  that follow the Kennicutt–Schmidt law.

While we have not attempted to measure the redshifts of the remaining high surface-brightness sources in our sample, the majority of objects with  $\mu_V < 26.0 \text{ mag arcsec}^{-2}$  are likely to be faint blue galaxies with  $z < 1.5$ . This conclusion is based on the luminosity function presented by Blanton et al. (2005), which includes a double Schechter function to account for the steep rise in galaxy density at the faint end. At  $r' = 28$  about 10 % will be at  $z > 3$ , with a median redshift of  $z = 1$ , while at  $r'=30$  about 30% will be at  $z > 3$  with a median redshift of 1.5. These numbers are relevant to the F606W image because its wavelength centroid is similar to that of the  $r'$  filter.

To increase the probability for detecting extended low surface brightness objects, we searched the masked F606W image by convolving it with smoothing kernels matched to a range of predicted  $\theta_{\text{dla}}$ 's, from  $\theta_{\text{dla}}=0.25''$  to  $\theta_{\text{dla}}=4.0''$  (see § 2.2). The number of objects found in the smoothed images versus the smoothing kernel size is presented in Fig. 3. The figure shows that the number of detected objects decreases rapidly with increasing  $\theta_{\text{kern}}$ : while 166 objects are detected when  $\theta_{\text{kern}}=0.25''$ , only one object is found when  $\theta_{\text{kern}}=1.0''$ , and *no objects are found for  $\theta_{\text{kern}} > 1.0''$* . In § 3.3 we shall argue that the steep fall off with  $\theta_{\text{kern}}$  indicates the presence of compact sources with light profiles that decline steeply with radius.

The implication is that spatially extended sources of low surface-brightness emission are rare in the UDF. Fig. 4 displays multi-color images of the 12 objects detected for  $\theta_{\text{kern}}=0.5''$ . Comparison between the smoothed and unsmoothed F606W image demonstrates the efficiency of the matched kernel technique for detecting extended objects that are exceedingly faint. The detection of objects with  $\theta_{\text{kern}} = 0.5''$  supports the conclusion that had they been present, faint objects with  $\theta_{\text{dla}} > 1''$  would also have been detected with kernels appropriately matched to  $\theta_{\text{dla}}$ . Lacking photometric redshifts, one cannot determine the nature of the 12 objects but it is likely that they are low surface-brightness dwarf galaxies at redshifts  $z \sim 1$ . The blue colors, central surface brightnesses, and linear diameters of the sample compiled by van Zee et al. (1997) would give rise to  $V$  band magnitudes, surface brightnesses, and angular diameters similar to those detected here, if the sample were redshifted to  $z \approx 1$ . Because of the similarity in  $V$  magnitudes, we also considered whether our detected objects belong to the class of IRAC selected galaxies found in the UDF by Yan et al. (2002). But this is unlikely since the IRAC galaxies are brighter at  $z_{850,AB}$  magnitude than at  $V$ , whereas all of the objects that we detected in  $V$  with  $\theta_{\text{kern}}=0.25''$  to  $1.0''$  are either fainter or undetected in  $z_{850,AB}$ . As a result, the density obtained by assuming these objects are in the redshift interval  $z=[2.5,3.5]$  acts as a conservative upper limit to the density of DLAs with

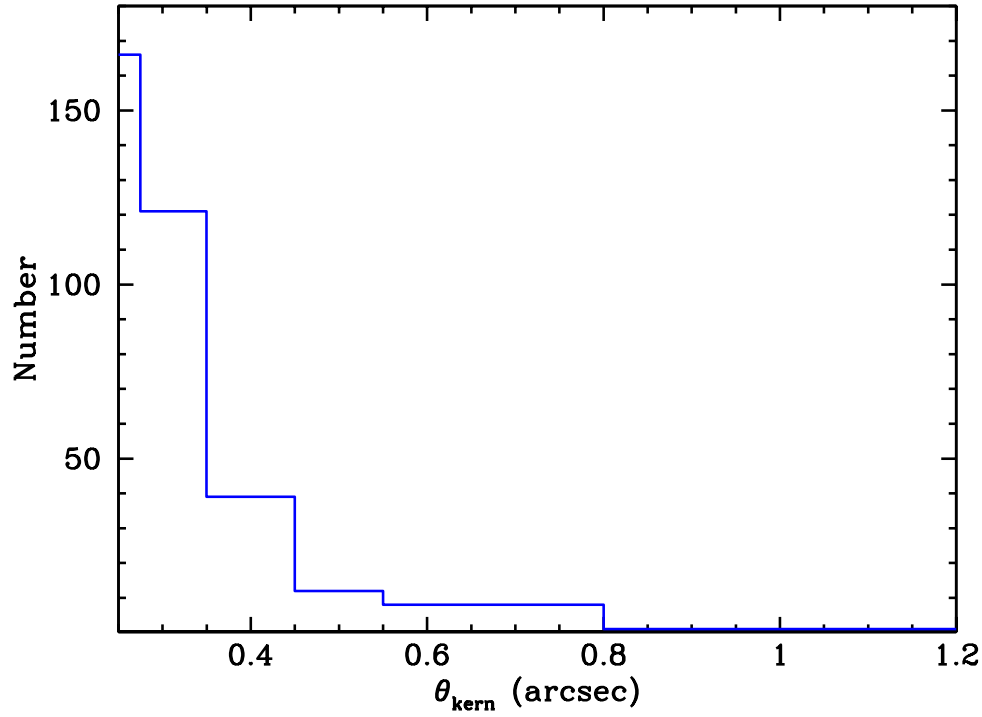


Fig. 3.— Histogram showing number of recovered DLAs as a function of  $\theta_{\text{kern}}$ . Step decrease with increasing  $\theta_{\text{kern}}$  indicates that increase in aperture size results in increase in sky noise but not in signal. This implies the predominance of compact galaxy light profiles reminiscent of dwarf galaxies at intermediate redshift. Part of fall-off is also due to the observed intrinsic decrease in galaxy counts with increasing flux.

$\theta_{\text{dla}}=0.5''$  in the same redshift interval. Similar conclusions hold for all DLAs with  $\theta_{\text{dla}} \leq 1''$ .

Therefore, in the cases of null detections,  $\theta_{\text{dla}} > 1''$ , we use cumulative Poisson probabilities to place a 95% confidence upper limit on  $\mathcal{N}$  of  $\mathcal{N}_{95} = 3$  for the number of low surface-brightness DLAs populating the UDF in the redshift interval  $z = [2.5, 3.5]$ . In the case of a single detection,  $\theta_{\text{dla}} = 1''$ , we place a corresponding 95 % confidence upper limit of  $\mathcal{N}_{95} = 4.7$ . For the multiple detections at  $\theta_{\text{dla}} < 1''$ , the values of  $\mathcal{N}_{95}$  are given in Table 1. We emphasize that the upper limits on  $\mathcal{N}$  are valid only for objects brighter than some threshold magnitude and surface brightness, which we determined by a Monte-Carlo technique described in the following subsection (§ 3.3).

### 3.3. Search Completeness

To determine the sensitivity of our searches for extended low surface-brightness objects, we performed a series of Monte-Carlo simulations. First, we generated test objects of different brightnesses for exponential light profiles of different scale-lengths. The angular exponential scale-lengths  $r_s$  were adjusted such that the FWHM ( $\equiv [2 \ln 2] r_s$ ) =  $\theta_{\text{dla}}$ . Next, we placed the test objects of a given magnitude and scale-length at 1000 random positions in the masked-F606W image, and smoothed the images with kernels in which  $\theta_{\text{kern}} = \theta_{\text{dla}}$  in the optimal case of matched kernels. Finally, we performed the detection procedure following the same detection algorithm described in § 3.1 for finding low surface brightness objects. We also repeated the simulations in which the synthetic galaxy light profiles were elliptical exponentials with  $b/a=0.5$  and with position angles varying between  $0^\circ$  and  $90^\circ$ : the difference with results for circular apertures was insignificant.

We measured the photometric properties of the recovered galaxies and computed the recovery fraction,  $\epsilon$ . This procedure was repeated by increasing the input magnitude  $V^{in}$  until the recovered number of galaxies decreased to some critical value. The results of this procedure are illustrated in Fig. 5, which plots  $\epsilon$  versus  $V^{in}$ . In principle one could determine the threshold value of  $V$  by raising  $V^{in}$  until only  $\mathcal{N}_{95}$  objects are left in the image. For those cases where  $\mathcal{N}_{95} \ll 200$  (i.e.  $\epsilon \ll 0.2$ ) we found that the measured magnitudes,  $V^{meas}$ , were sufficiently faint that overlap between the synthetic galaxies and the low-surface brightness wings extending from the masked real galaxies led to spurious over-estimates in flux determinations for the synthetic galaxies (in most cases this effect results in  $V^{meas}$  to be brighter than  $V^{in}$ ). This is evident in the saturation of the  $\epsilon$  versus  $V^{in}$  curves in Fig. 5: the flattening at  $\epsilon < 0.2$  for  $\theta_{\text{dla}}=4''$  and at  $\epsilon < 0.1$  for the other values of  $\theta_{\text{dla}}$  illustrates this effect. On the other hand when  $\epsilon \geq 0.2$ , the  $V^{in}$  were sufficiently bright that the output  $V^{meas}$  were reliable. As a result we assume the threshold magnitude is given by  $V^{in}$  for  $\epsilon = 0.2$  and the threshold surface brightness is given by the corresponding value of  $\mu_V^{in}$  (hereafter

Fig. 4a.— multi-band images of galaxies detected with  $0.5''$  kernel. Column 1 shows smoothed F606 W image, col. 2 shows F606W masked image. Remaining columns show unsmoothed images for designated filters. Images are  $5''$  on each side.

Fig. 4b.— Same as 4a

Fig. 4c.— Same as 4a

$r_s^a$ arcsec	$\theta_{\text{kern}}^b$ arcsec	$\mathcal{N}_{\text{det}}^c$	$\mathcal{N}_{95}^d$	$V^{\text{thresh}}^e$ mag	$\mu_V^{\text{thresh}}^f$ mag arcsec <sup>-2</sup>	SFR <sup>g</sup> M <sub>⊙</sub> yr <sup>-1</sup>	$\log(\dot{\psi}_*)^{\text{thresh}}^h$ M <sub>⊙</sub> yr <sup>-1</sup> kpc <sup>-2</sup>	$\log \dot{\rho}_*^i$ M <sub>⊙</sub> yr <sup>-1</sup> Mpc <sup>-3</sup>
(1)	(2)	(3)	(4)	(5)	(6)	(7)	(8)	(9)
0.18	0.25	166	<186	....	28.0	14.0	-1.73	-3.31
0.22	0.3	121	<141	....	28.1	13.5	-1.77	-3.32
0.29	0.4	39	<50.9	....	28.5	7.15	-1.93	-3.59
0.36	0.5	12	<19.4	....	28.7	2.91	-2.01	-3.84
0.43	0.6	8	<14.4	....	28.9	2.76	-2.09	-3.81
0.72	1.0	1	<4.7	....	29.3	0.66	-2.25	-4.09
1.44	2.0	0	<3	26.5	29.8	2.86	-2.45	-3.58
2.89	4.0	0	<3	25.0	29.7	11.7	-2.41	-2.97

Table 1: Results of UDF Search in F606W Image

<sup>a</sup>Light profile exponential scale-length for synthetic galaxy used to compute threshold value of  $\dot{\psi}_*$  for all cases and threshold  $\dot{\rho}_*$  in the case of null detections.

<sup>b</sup>FWHM of Gaussian smoothing kernel

<sup>c</sup>Number of objects detected in the UDF with given value of  $\theta_{\text{kern}}$

<sup>d</sup>95 % confidence upper limit on number of objects in UDF with given  $\theta_{\text{kern}}$

<sup>e</sup>Threshold input  $V$  magnitude, when  $\epsilon=0.2$ . Used to compute upper limits on SFRs for kernels with null detections. Not used for kernels with positive detections.

<sup>f</sup>Threshold input  $V$  band surface brightness when  $\epsilon=0.2$

<sup>g</sup>Upper limit on SFR. For  $\mathcal{N}_{\text{det}} = 0$  this corresponds to threshold  $V$  magnitude, and for  $\mathcal{N}_{\text{det}} \neq 0$  this corresponds the SFR averaged over the  $\mathcal{N}_{\text{det}}$  galaxies.

<sup>h</sup>Lower limit on  $\dot{\psi}_*(z=3.5)$  corresponding to threshold  $\mu_V$

<sup>i</sup>95 % confidence upper limit on  $\dot{\rho}_*$

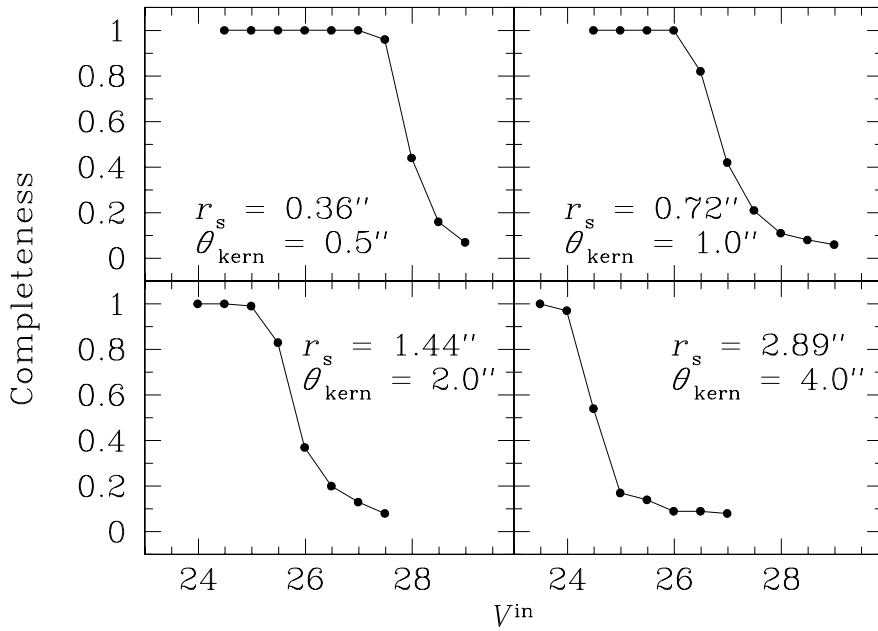


Fig. 5.— Recovery fraction  $\epsilon$  versus input magnitude  $V^{in}$  for increasing values of  $\theta_{\text{kern}}$  for the matched kernel condition,  $\theta_{\text{kern}} = \theta_{\text{dla}}$ . Notice how  $V^{in}$  at a given recovery fraction,  $\epsilon = 0.2$ , decreases with increasing  $\theta_{\text{kern}}$ . This results from noise increase due to increase in aperture size. The flattening observed at  $\epsilon = 0.2$  is due overlapping of synthetic galaxy profiles with low brightness wings extending from masked galaxies.

we refer to these as  $V^{thresh}$  and  $\mu_V^{thresh}$ ). We emphasize that the  $\epsilon=0.2$  criterion is conservative as it requires the detection of 200 objects, which exceeds  $\mathcal{N}_{95}$  for all values of  $\theta_{\text{dla}}$ . The resulting threshold magnitudes and surface brightnesses corresponding to the values of  $\theta_{\text{kern}}$  used for galaxy detection are shown in Table 1.

A possible concern over this procedure arises from our use of  $10^3$  synthetic galaxies even though Fig. 2 shows that  $\mathcal{N}$ , the number of DLAs predicted for the UDF, can be as large as  $10^5$ . However, the threshold values of  $V^{in}$  and  $\mu_V^{in}$  inferred from the simulations are independent of  $\mathcal{N}$ . The reason is that confusion noise due to fluctuations in the number of synthetic galaxies per aperture beam does not increase with increasing  $\mathcal{N}$ : for DLAs with a fixed area covering factor  $f_A(\text{DLA})$  the number of galaxies per “beam” area,  $\pi\theta_{\text{kern}}^2/4$ , equals  $f_A(\text{DLA})(\theta_{\text{kern}}/\theta_{\text{dla}})^2$ , which is independent of  $\mathcal{N}$  and is less than 1 for the case of matched kernels assumed here. Other systematic errors such as that due to overlap between the galaxy light profiles is negligible because the area covering factor of 200 synthetic galaxies is less than 6 %. Therefore, the principal systematic error in determining the thresholds is caused by overlap between the synthetic light profiles and the faint wings of masked real galaxies (see above).

We next used the simulations to interpret the steep fall-off in the number of detected galaxies with  $\theta_{\text{kern}}$  (Fig. 3). Part of the fall-off is due to the loss of sensitivity resulting from the increase of  $\theta_{\text{kern}}$  above  $\theta_{\text{dla}}$ . This is illustrated in Fig. 6, which shows that  $V^{thresh}$  decreases with increasing  $\theta_{\text{kern}}$  for  $\theta_{\text{kern}} > \theta_{\text{dla}}$ . Therefore, a loss of sources will result from a decrease in survey depth with increasing  $\theta_{\text{kern}}$ . A fall off of sources with decreasing  $V^{thresh}$  can also be attributed to the intrinsic shape of the source counts-magnitude relation. From known field number counts (Metcalf et al. 20001), we estimate that for every half magnitude deeper, we gain about 20% more objects at  $V \sim 28$ . If we adopt this rate and our survey depth estimated from an exponential profile, which went from  $V^{thresh}=29.0$  to  $V^{thresh}=28.7$  when we increase the smoothing kernel size from  $0.3''$  to  $0.4''$ , we estimate a loss of only about 13 % of the targets if the decline is due to survey depth alone. Because Fig. 3 indicates a more significant drop than this, we suggest within one exponential scale length the intrinsic light profiles of the detected galaxies are steeper than an exponential function, which is consistent with the dwarf galaxy hypothesis.

### 3.4. Estimated Comoving SFR Densities

We computed empirical upper limits on  $\dot{\rho}_*(\geq\dot{\psi}_*)$  in the following manner. First, in the case of null detections,  $\theta_{\text{kern}}=2''$  and  $4''$ , we used the threshold magnitudes  $V^{thresh}$  in Table 1 to determine the minimum luminosity,  $L_V^{min}$  detectable out to  $z_{\text{high}}=3.5$ . We then converted  $L_V^{min}$  into a SFR by assuming  $\text{SFR}=1.25\times 10^{-28}L_V^{min}$  (Madau et al. 1998), and let  $\dot{\rho}_*=\mathcal{N}_{95}\times\text{SFR}/\Delta V_{\text{co}}$  to find the 95% confidence upper limit on  $\dot{\rho}_*$ , where  $\Delta V_{\text{co}}$ , the comoving volume of the UDF, equals  $3.3\times 10^4$   $\text{Mpc}^3$  for the redshift interval  $z=[2.5,3.5]$ . We then used Eq. 3 to compute the threshold value of  $\dot{\psi}_*$  from the threshold surface brightnesses  $\mu_V^{thresh}$  in Table 1. The resulting  $\dot{\rho}_*(\geq\dot{\psi}_*)$  are plotted in Fig. 7 and entered in Table 2 for both values of  $\theta_{\text{kern}}$ . In the case of positive detections,  $\theta_{\text{kern}} < 1''$ ,



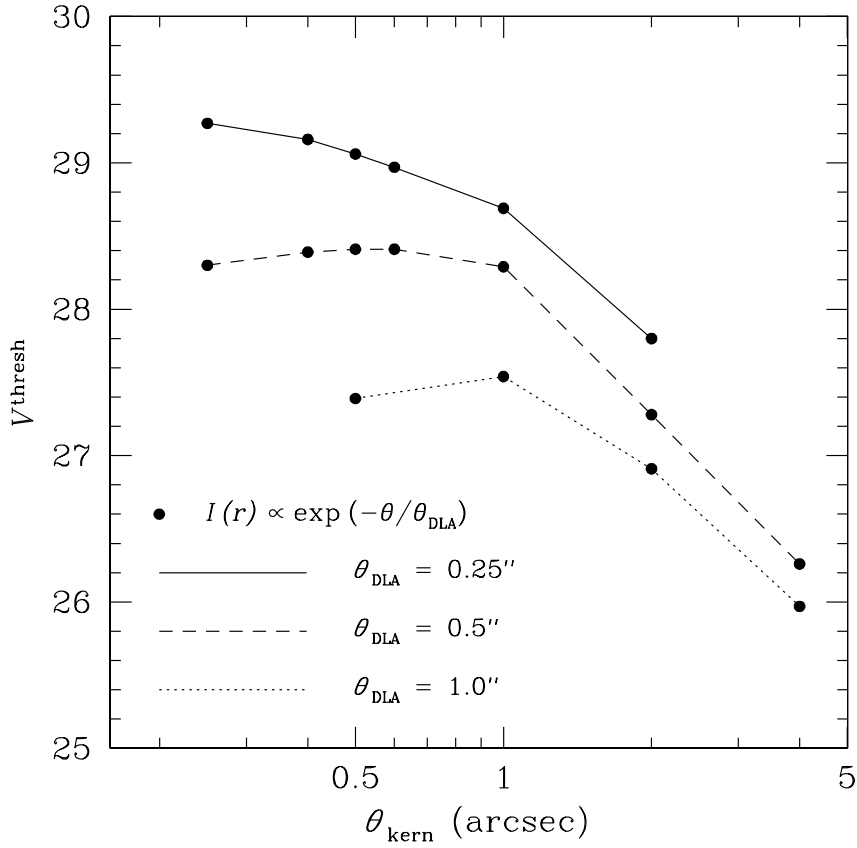


Fig. 6.— Threshold magnitude  $V^{\text{thresh}}$  versus  $\theta_{\text{kern}}$  for fixed DLA diameters,  $\theta_{\text{dla}} = 0.25''$ ,  $0.5''$ , and  $1.0''$ . Decrease of  $V^{\text{thresh}}$  with increasing  $\theta_{\text{kern}}$  at  $\theta_{\text{kern}} \geq \theta_{\text{dla}}$  due to increase in sky noise in larger apertures. Decrease of  $V^{\text{thresh}}$  with decrease in  $\theta_{\text{kern}}$  at  $\theta_{\text{kern}} < \theta_{\text{dla}}$  due to effect of smoothing kernel alone.

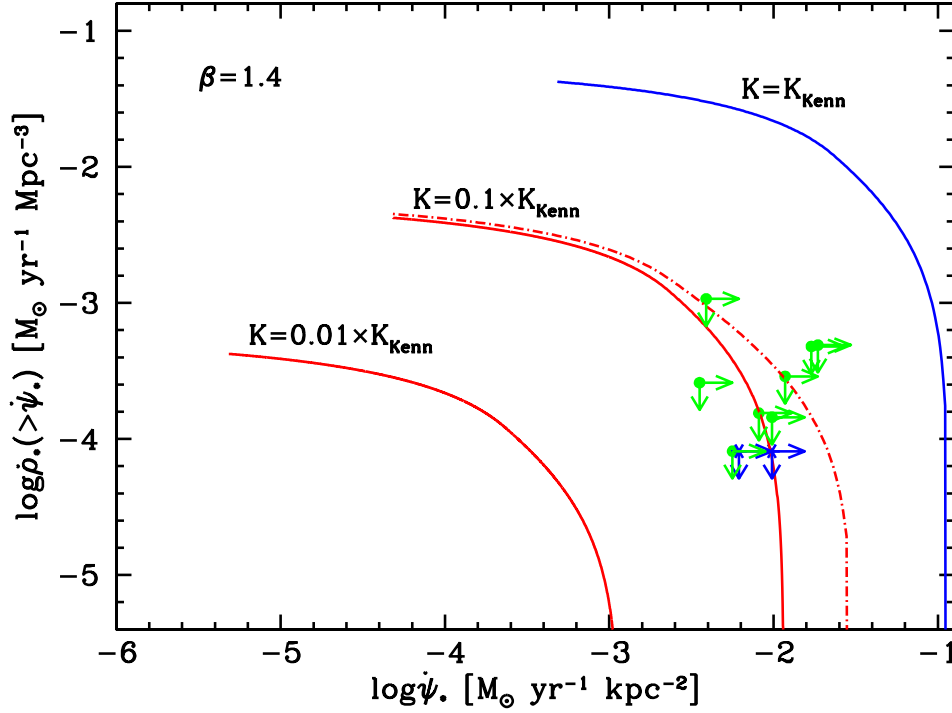


Fig. 7.— Cumulative comoving SFR densities versus  $\dot{\psi}_*$ . Green data points correspond to upper limits derived for  $\theta_{\text{kern}}=4''$ ,  $2''$ ,  $1''$ ,  $0.6''$ ,  $0.5''$ ,  $0.4''$ ,  $0.3''$ , and  $0.25''$  in counter-clockwise order starting with  $(\log \dot{\psi}_*, \log \dot{\rho}_*)=(-2.41, -2.97)$ : matched kernels assumed in deriving SFR thresholds. Blue (starred) data points correspond to unmatched kernel with  $\theta_{\text{dla}}=1.0''$  and  $\theta_{\text{kern}} = 0.5''$  and  $2.0''$  in order of increasing  $\dot{\psi}_*$ . Blue curve is  $\dot{\rho}_*(\geq \dot{\psi}_*)$  predicted for Kennicutt-Schmidt law with  $K=K_{\text{Kenn}}$ . Solid Red curves are for  $K=0.1K_{\text{Kenn}}$  and  $K=0.01K_{\text{Kenn}}$ . The range of  $\dot{\psi}_*$  for all solid curves corresponds to  $N=[2 \times 10^{20}, 1 \times 10^{22}]$ . Dot-dashed red curve is same as solid red curve for  $K=0.1K_{\text{Kenn}}$  except that  $N_{\text{max}}=2 \times 10^{22} \text{ cm}^{-2}$ .

we assumed all the detected objects were at  $z=3$  (since the average redshift of all of the detected objects is more likely to equal the average redshift rather than the maximum redshift,  $z_{high}$ , of the UDF search volume) and added the inferred values of  $L_\nu$  to obtain the total SFR. Because  $\mathcal{N}_{95}$  exceeds the number of detected galaxies,  $\mathcal{N}_{det}$ , the luminosities of the  $\mathcal{N}_{95} - \mathcal{N}_{det}$  galaxies are unknown. We addressed this issue by assigning the mean SFR of the detected sample  $\langle \text{SFR} \rangle$  to each excess galaxy. Therefore, in these cases  $\dot{\rho}_* = \mathcal{N}_{95} \langle \text{SFR} \rangle / \Delta V_{co}$ . Note, whereas the threshold values of  $\dot{\psi}_*$  were computed with the same method used in the case of null detections, in this case the limits on  $\dot{\rho}_*$  depend on the  $V$  magnitudes measured for each detected galaxy rather than on the value of  $V^{thresh}$  used in the case of null detections.

We wish to comment on two more points about Fig. 7. First, the horizontal green arrows directed toward increasing  $\dot{\psi}_*$  emphasize that each upper limit on  $\dot{\rho}_* (\geq \dot{\psi}_*)$  is valid for projected SFRs  $\geq \dot{\psi}_*$ . Second, the upper limits on  $\dot{\rho}_*$  decrease with decreasing  $\theta_{kern}$  between  $\theta_{kern} = 4.0''$  and  $1.0''$  because  $\mathcal{N}_{95}$  is essentially unchanged while the sky noise contribution to the measured flux is diminished in the smaller kernels. This is reversed to an increase in  $\dot{\rho}_*$  with decreasing  $\theta_{kern}$  for  $\theta_{kern} < 1.0''$  because the rapid rise in  $\mathcal{N}_{95}$  with decreasing  $\theta_{kern}$  (Fig.3) offsets the reduction in sky noise. The corresponding  $\dot{\psi}_*$  coordinate increases with decreasing  $\theta_{kern}$  in every case due to the increased error in surface brightness with decreasing  $\theta_{kern}$ .

#### 4. DISCUSSION OF RESULTS

The most striking feature of Fig. 7 is that the comoving SFR densities predicted by the local Kennicutt-Schmidt law (the blue curve) exceed the 95 % confidence upper limits established for the UDF by at least a factor of 30 for  $\theta_{kern} = 0.25''$ ,  $0.30''$ , and  $4.0''$ , and by more than a factor of 100 for other values of  $\theta_{kern}$ .

We believe these discrepancies are real for the following reasons.

(1) the discrepancy is established for a wide range of  $\theta_{kern}$  values, indicating the results are not overly sensitive to the values of  $\theta_{dla}$ .

(2) The upper limits are likely to be conservative; i.e., the locations of the data points are likely to occur at values of  $\dot{\psi}_*$  and  $\dot{\rho}_*$  lower than in Fig. 7. In the case of null detections,  $\theta_{kern} = 2.0''$  and  $4.0''$ , the location of the upper limits in the  $\dot{\psi}_*, \dot{\rho}_*$  plane were determined by the threshold surface brightnesses and magnitudes determined in our simulations. In § 3.3 we discussed why our recovery criterion of 200 objects led to large values of  $\dot{\psi}_*$  and  $\dot{\rho}_*$ . In the case of positive detections,  $\theta_{kern} \leq 1.0''$ , the threshold values of  $\dot{\psi}_*$  are again determined by the simulations, but the upper limits on  $\dot{\rho}_*$  are set by the magnitude determinations of the detected objects. Because a significant fraction of these objects are likely to be intermediate-redshift dwarf galaxies, the contribution of all the detections to the total SFR in  $\Delta V_{co}$  is a conservative upper limit.

(3) The discrepancy is not overly sensitive to the matched-kernel assumption described in § 3.

The two blue stars in Fig. 3 correspond to  $\dot{\psi}_*$  and  $\dot{\rho}_*$  inferred for  $\theta_{\text{dla}}=1''$  and  $\theta_{\text{kern}} = 0.5''$  and  $2.0''$ . The small changes in threshold  $\dot{\psi}_*$  support our conclusion that the discrepancy between empirical and predicted estimates in the  $\dot{\psi}_*, \dot{\rho}_*$  plane is robust.

(4) Each of the upper limits on  $\dot{\rho}_*$  in (Fig. 7) applies to DLAs of the same size. But in a realistic scenario, DLAs contributing to  $\dot{\rho}_*$  would span some range in size (or in mass since size is correlated with dark-matter mass in most models). Springel & Hernquist (2003) found that  $\dot{\rho}_* = \Omega_M \rho_{\text{crit}} \int_0^\infty S(M, z) dM$  where  $\rho_{\text{crit}}$  is the current critical cosmological density and the multiplicity function  $S(M, z)$  is the product of the comoving density of dark-matter halos and the SFR per unit halo mass. Therefore, the SFR density predicted for a given smoothing kernel is given by  $(\dot{\rho}_*)_{\theta_{\text{kern}}} = [\int_{M_-}^{M_+} S(M, z) dM / \int_0^\infty S(M, z) dM] \dot{\rho}_*$  where  $M_-$  and  $M_+$  are the mass limits corresponding to the range in  $\theta_{\text{dla}}$  detectable with a given  $\theta_{\text{kern}}$ . As a result the only relevant upper limits are those corresponding to kernels sensitive to masses contributing the bulk of the predicted  $\dot{\rho}_*$ ; i.e., kernels for which  $(\dot{\rho}_*)_{\theta_{\text{kern}}}$  is not much less than  $\dot{\rho}_*$ . Our simulations indicate that the smoothing kernels maintain maximal sensitivity for DLAs with  $\theta_{\text{dla}} = (0.5 \rightarrow 1.5) \theta_{\text{kern}}$ . Thus, the kernel with  $\theta_{\text{kern}} = 2''$  is sensitive to  $z=3$  DLAs with  $d_{\text{dla}} = 8 \text{ kpc}$  to  $24 \text{ kpc}$ . In the spherical collapse model the corresponding range in dark-matter masses is  $10^{11} M_\odot$  to  $10^{13} M_\odot$  if we assume the virial radius  $r_{200} \approx 10(d_{\text{dla}}/2)$  (see § 5.1). Fig. 9 in Springel & Hernquist indicates that halos in this mass range contribute about 50 % of the predicted  $\dot{\rho}_*$  at  $z=3$ . This model would be ruled out by our data since the predicted  $\dot{\rho}_*$  is 100 times larger than the empirical upper limit for  $\theta_{\text{kern}} = 2''$ . While more rigorous methods are needed to verify this result, our preliminary analysis indicates that the results presented here are valid in the case of distributed DLA sizes.

(5) The values of  $\dot{\rho}_*(\geq \dot{\psi}_*)$  predicted for the local Kennicutt parameters,  $K$  and  $\beta$ , are likely to be higher than depicted by the blue curve in Fig. 7. While the predicted  $\dot{\rho}_*(\geq \dot{\psi}_*)$  is well determined by the accurately measured parameters such as the slope  $\alpha_3$ , normalization  $k_3$ , and turn-over column density  $N_d$ , it also depends on the uncertain value of  $N_{\text{max}}$ . We chose  $N_{\text{max}} = 1 \times 10^{22} \text{ cm}^{-2}$  because the largest measured column density in the SDSS sample is  $N = 8 \times 10^{21} \text{ cm}^{-2}$  (PHW05). The blue curve is a lower limit because  $\dot{\rho}_*(\geq \dot{\psi}_*)$  would increase if  $N_{\text{max}}$  were raised above  $1 \times 10^{22} \text{ cm}^{-2}$ , which cannot be ruled out. Furthermore the predicted  $\dot{\rho}_*(\geq \dot{\psi}_*)$  would also increase if DLAs are not the planar objects assumed in § 2,

(6) A potential problem with our results is that while the UDF measurements sample scales exceeding 1 kpc, the expression for  $\dot{\rho}_*$  in Eq. 6 depends on  $f(N, X)$  which is based on absorption-line measurements that sample scales  $\sim 1 \text{ pc}$  (Lanzetta et al. 2002). The difficulty is that the Kennicutt-Schmidt law has been established only on scales exceeding 0.3 kpc (Kennicutt et al. 2005). However, because  $f(N, X)$  typically depends on over 50 measurements per column-density bin of width  $\Delta \log N = 0.1$  (PHW05), Eq. 5 implies that the corresponding comoving SFR density  $\Delta \dot{\rho}_*$  is a statistical average over the differential area  $\Delta A \approx (H_0/c) f(N, X) \Delta N / n_{\text{co}}$  (assuming spherical symmetry). We find that  $\Delta A \approx 0.5(N_d/N)(\theta_{\text{dla}}/1 \text{ arcsec})^2 \text{ kpc}^2$ . As a result  $\Delta A \approx 2 \text{ kpc}^2$  for  $\theta_{\text{dla}} = 1''$  at the median DLA column density  $N = 8 \times 10^{20} \text{ cm}^{-2}$ . Since our calculation corresponds to the cumulative quantity  $\dot{\rho}_*(>N)$ , the effective statistical area probed by our expression will

exceed a few kpc<sup>2</sup>. Therefore, while individual measurements sample scales less than 1 pc,  $\dot{\rho}_*$  is statistically established on scales for which the Kennicutt-Schmidt law has been established at  $z=0$ .

## 5. IMPLICATIONS

The discrepancies with predictions by the Kennicutt-Schmidt law have implications for the efficiency of star formation in DLAs. They also have broader implications concerning metal production and energy balance in DLAs and their relationship to LBGs. We discuss each of these topics in turn.

### 5.1. Star Formation Efficiency in DLAs

The discrepancy between predicted and measured values of  $\dot{\rho}_*$  suggests that star formation is less efficient in DLAs; i.e., for a given  $N$ ,  $\dot{\psi}_*$  in DLAs is lower than in nearby galaxies. This point is illustrated by the solid red curves in Fig. 7, for which the Kennicutt parameter  $K$  is reduced by factors of 10 and 100 below the local value,  $K=K_{Kenn}$ . As  $K$  decreases, the solutions shift toward decreasing  $\dot{\psi}_*$  and  $\dot{\rho}_*$  along a 45° diagonal in the  $(\log\dot{\psi}_*, \log\dot{\rho}_*)$  plane as both  $\dot{\psi}_*$  and  $\dot{\rho}_*$  are proportional to  $K$ . Because the upper limits on  $\dot{\rho}_*$  apply only to projected SFRs above the  $\dot{\psi}_*$  thresholds, Fig. 7 shows that  $K$  need not be reduced by much more than by a factor of 10 to obtain agreement between theory and all the data points. Further reductions are unnecessary since they shift the predicted  $\dot{\rho}_*(\geq\dot{\psi}_*)$  curves below the  $\dot{\psi}_*$  thresholds. Nevertheless  $K$  must be reduced by *at least* a factor of 10. This is illustrated by the dashed red curve in Fig. 7, which shows that  $\dot{\rho}_*(\geq\dot{\psi}_*)$  predicted for  $K = 0.1 \times K_{Kenn}$  is incompatible with all the upper limits other than those corresponding to  $\theta_{\text{kernel}} = 0.25''$  and  $0.30''$  when  $N_{\text{max}}$  is increased to  $2 \times 10^{22} \text{ cm}^{-2}$ .

The SFR efficiencies can also be decreased by lowering the slope  $\beta$  of the Kennicutt-Schmidt law, while keeping  $K=K_{Kenn}$ . Although Kennicutt (1998a) found  $\beta=1.40 \pm 0.15$  when he compared projected SFRs with the total gas column densities for a sample of 60 galaxies, Gao & Solomon (2004) found  $\beta=1$  by comparing the SFRs with the H<sub>2</sub> column densities of 32 galaxies. Because our knowledge of physical conditions in high- $z$  gas is limited, we cannot rule out the possibility that  $\beta = 1$  also holds for the atomic gas content of DLAs. Fig. 8 compares the  $\dot{\rho}_*(\geq\dot{\psi}_*)$  curves predicted for  $\beta = 1$  and  $\beta = 0.6$  with the standard case,  $\beta=1.4$ . With the possible exception of DLAs with  $\theta_{\text{dla}}=0.25''$ , the curves predicted for  $\beta=1$  are inconsistent with the data. Fig. 8 also shows consistency with all the data points is achieved if  $\beta \leq 0.6$ . While we cannot rule out such low values entirely, the cases  $\beta=1.0$  or  $1.4$  are at least physically motivated (see Elmegreen 2002 and Kravtsov 2003). Because we are unaware of any evidence or physical argument to justify values of  $\beta$  less than 0.6, we focus instead on other mechanisms for reducing SFR efficiencies in DLAs.

The SFRs would be reduced if the critical surface density for the Kennicutt-Schmidt law (see Eq. 1) were higher in DLAs. The physical basis for this follows from the Toomre instability

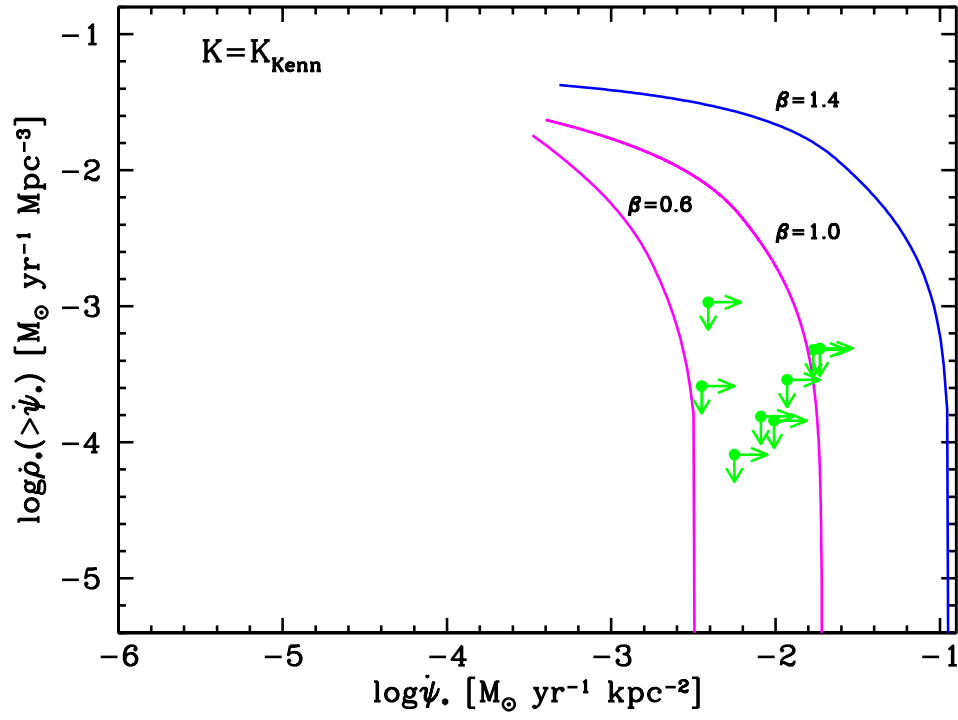


Fig. 8.— Cumulative comoving SFR density versus  $\dot{\psi}_*$ . Data points as in Fig. 7. Theoretical curves correspond to  $K = K_{\text{Kenn}}$  for slopes  $\beta = 1.4, 1.0,$  and  $0.6$ .

criterion, which is characterized by the parameter  $Q = \kappa\sigma_g/\pi G\mu m_H N_\perp$  (Toomre 1964), where  $\sigma_g$  is the gas velocity dispersion, and  $\kappa$  is the epicyclic frequency. The critical H I column density,  $N_\perp^{crit} = \kappa\sigma_g/\pi G\mu m_H$ , is set by the condition  $Q=1$ : gas with  $N_\perp > N_\perp^{crit}$  is unstable to collapse and possible subsequent star formation, while gas with  $N_\perp \leq N_\perp^{crit}$  is stable. In a disk with a flat rotation curve  $\kappa(r) = \sqrt{2}v_{rot}/r$ , where  $r$  is radial distance from the center of the disk and  $v_{rot}$  is the rotation speed. Following Kauffmann (1996) and Mo et al. (1998) we assume the DLA disk radius  $r_{dla} \approx 0.1r_{200}$  where  $r_{200}$  is essentially the virial radius of the dark-matter halo enclosing the disk and  $r_{dla}$  is defined by the condition  $N(r_{dla}) = N_{min} = 2 \times 10^{20} \text{ cm}^{-2}$ . Adopting the spherical collapse model for disk formation, one finds  $v_{rot}/r_{200} = 10H(z)$  (Mo et al. 1998) where  $H(z)$  is the Hubble parameter. The presence of the  $H(z)$  term implies that  $N_\perp(r)$  at  $z=3$  must be at least a factor of 5 higher than at  $z=0$  for gas to form stars. Specifically,  $N_\perp(r)$  must exceed  $N_\perp^{crit}(r) = 2.2 \times 10^{21} (r_{dla}/r) \text{ cm}^{-2}$  for gas at radius  $r$  to be Toomre unstable when  $z = 3$ . But the double power-law form of  $f(N, X)$  rather indicates the gas is stable. For randomly oriented disks, the break of the double power-law occurs at  $N_d = N_0$  where  $N_0$  is the maximum value of  $N_\perp(r)$ : in § 2.1 we found that  $N_d = 3.16 \times 10^{21} \text{ cm}^{-2}$ . Combining Eqs. 5 and 8 with the solution  $g(N_\perp, X) = k_3(N_\perp/N_0)^{-2}$ , we find that  $N_\perp(r) = N_0 \left[ 1 + 20[(r^2 - r_0^2)/r_{dla}^2] \right]^{-1}$  for  $r_0 < r < r_{dla}$  where  $r_0$  satisfies the condition  $N_\perp(r_0) = N_0$ . Comparison with  $N_\perp^{crit}(r)$  shows that  $N_\perp(r) < N_\perp^{crit}(r)$  for all solutions in which  $N_\perp(r_{dla}) < N_{min}$ . Therefore, *in situ* star formation in DLAs may be suppressed because they are subcritical disks.

On the other hand the uncertainties in our model assumptions lead to uncertainties in the values of  $N_\perp^{crit}$ . Moreover, uncertainties in the slope  $\alpha_4 \equiv d \log f(N, X) / d \log N$  at  $N \geq N_d$  indicate that the disk hypothesis, which predicts  $\alpha_4 = -3$ , is not well established (see §2.1). Therefore, gravitationally unstable gas with  $N > 3.16 \times 10^{21} \text{ cm}^{-2}$  may be present in DLAs. As a result, while cosmological evolution may be an important factor in rendering DLA gas subcritical, additional factors may be needed to suppress star formation at column densities up to  $10^{22} \text{ cm}^{-2}$ . One such factor may be the low molecular content of DLAs: molecules are crucial for star formation since emission from rotational transitions of CO and other molecules enables clouds to cool below the atomic lower limit of  $\sim 100 \text{ K}$  and to ultimately collapse and form stars. Whereas the median  $\text{H}_2$  content in the diffuse neutral gas of the Galaxy,  $f_{\text{H}_2} \approx 10^{-1}$  (Tumlinson et al. 2002), Ledoux et al. (2003) find that  $f_{\text{H}_2} < 10^{-6}$  in DLAs. Interestingly, the median values for  $f_{\text{H}_2}$  in the LMC and SMC are less than  $10^{-4}$ . Tumlinson et al. (2002) argue that the low molecular content of the LMC and SMC is likely due to low dust content and relatively strong FUV radiation fields. Since the low dust level suppresses  $\text{H}_2$  formation on grains while the high FUV radiation level increases the  $\text{H}_2$  photodissociation rate, higher values of  $N$  are required for the gas to be self-shielding against photodissociating radiation. Because DLAs have lower dust-to-gas ratios than either the LMC or SMC but have similar FUV radiation fields (WPG03), the same mechanisms may be responsible for the low molecular content of DLAs. Calculations of photodissociation equilibrium suggest that  $f_{\text{H}_2}$  would be suppressed at  $N < 10^{22} \text{ cm}^{-2}$  in DLA gas (Tumlinson et al. 2002; Hirashita & Ferrara 2005). Krumholz & McKee (2006) and Blitz & Rosolowsky (2006) argue that  $\dot{\psi}_* \propto f_{\text{H}_2}$ ,

which would help to explain the factor of ten or more reduction in the efficiency of star formation in DLAs. Consequently, while gas in DLAs with  $N > N^{crit} < 10^{22} \text{ cm}^{-2}$  is Toomre unstable, it may be unable to collapse to form stars. This is in contrast to the Galaxy and most metal-rich spirals studied by Martin & Kennicutt (20001) in which the condition  $N > N^{crit}$  normally results in star formation. The explanation (R. C. Kennicutt 2006, priv. comm.) may be the result of a coincidence between  $N^{crit}$  and the column density at which molecular gas becomes self shielding. Because of its relatively high dust-to-gas ratio, this is lower in the Galaxy (and most metal-rich spirals) than in metal-poor objects such as the LMC, SMC (Tumlinson et al. 2002), and in DLAs. This may help to explain why the Toomre criterion alone appears to be a sufficient condition for the onset of star formation in most metal-rich spirals (Martin & Kennicutt 2001), but not in DLAs.

A further mechanism for cloud stabilization was suggested by Ferguson et al. (1998) who argued that flaring of the H I disk in the outer regions of spiral galaxies leads to suppression of star formation: for a given gas surface density the increased scale-height reduces the volume density, which helps to stabilize gas against Jeans instability. Schaye (2004) argued that disks would be Toomre stable provided the gas is a warm ( $T \sim 10^4 \text{ K}$ ) neutral medium and unstable when the gas is a cold ( $T \sim 100\text{K}$ ) neutral medium. But independent lines of evidence (e.g. WGP03; Howk et al. 2005) suggest that half of the known sample of DLAs is comprised of cold ( $T \sim 100\text{K}$ ) gas with column densities exceeding the  $(5-20) \times 10^{20} \text{ cm}^{-2}$  instability threshold. While this mechanism needs to be investigated further, current evidence suggests that phase transitions alone are not sufficient to trigger star formation in DLAs. There may be other mechanisms that do suppress star formation, but further discussion is beyond the scope of this paper.

## 5.2. Implications for Metal Production and Heat Input: the LBG Connection

The UDF results place a conservative upper limit on  $\dot{\rho}_*$  contributed by DLAs with  $N \geq N_{min}$ , which is given by  $\dot{\rho}_* < 10^{-2.4} \text{ M}_\odot \text{ yr}^{-1} \text{ Mpc}^{-3}$  for  $z \approx 3$  (see curve with  $K=0.1 \times K_{Kenn}$  in Fig. 7). The new limit on  $\dot{\rho}_*$  has several consequences. First, since the metal production rate is proportional to  $\dot{\rho}_*$ , one can compute the DLA metallicity at a given redshift from the previous history of  $\dot{\rho}_*(z)$ . Nagamine et al. (2004b) used their numerical simulations, which incorporated the Kennicutt-Schmidt law, to predict  $\dot{\rho}_* = 10^{-1} \text{ M}_\odot \text{ yr}^{-1} \text{ Mpc}^{-3}$  and the metallicity  $[\text{M}/\text{H}] = -0.5$  at  $z=3$ . If we scale their result to our upper limit on  $\dot{\rho}_*$ , their chemical evolution model predicts  $[\text{M}/\text{H}] < -1.9$ . By comparison the average DLA metallicity at  $z \approx 3$  is given by  $[\text{M}/\text{H}] = -1.40 \pm 0.07$  (Prochaska et al. 2003). Therefore, our limit on  $\dot{\rho}_*$  has shifted the problem of metal overproduction by a factor of ten in DLAs (see WGP03) to one of underproduction a factor of three.

Second, the new limit on  $\dot{\rho}_*$  implies a gas heating rate significantly lower than indicated by the measured cooling rate. The [C II] 158  $\mu\text{m}$  cooling rate per unit comoving volume inferred from C II\* absorption in DLAs (Wolfe et al. 2004) is given by

$$\mathcal{C} = \Omega_g \rho_{crit} < \ell_c > / \mu m_H \quad , \quad (9)$$



where  $\Omega_g$  is the mass per unit comoving volume of neutral gas in DLAs,  $\langle \ell_c \rangle$  is the average [C II] 158  $\mu\text{m}$  cooling rate per H atom, and  $\mu m_H$  is the average mass per particle. Assuming  $\mu=1.3$ , our data indicate  $\mathcal{C} = (2 \pm 0.5) \times 10^{38} \text{ ergs s}^{-1} \text{ Mpc}^{-3}$  in the redshift interval  $z=[2.5, 3.5]$ . Here we have ignored half the DLA population with  $\ell_c < 10^{-27.1} \text{ ergs s}^{-1} \text{ H}^{-1}$  because it is likely heated by background radiation alone (Wolfe 2005).

To balance cooling, Wolfe et al. (2003a [hereafter WPG03]) suggested the grain photoelectric effect as a plausible heating mechanism. The comoving heating rate is given by

$$\mathcal{H} = \int \phi(L_\nu) H(L_\nu) dL_\nu \quad , \quad (10)$$

where  $\phi(L_\nu) dL_\nu$  is the comoving density of DLAs with FUV luminosities in the interval  $(L_\nu, L_\nu + dL_\nu)$ . The heating rate per DLA is given by

$$H(L_\nu) = \int \Gamma(\mathbf{r}) n(\mathbf{r}) dV \quad , \quad (11)$$

where  $\Gamma(\mathbf{r})$  is the heating rate per H atom,  $n(\mathbf{r})$  is the density of H atoms at displacement vector  $\mathbf{r}$ , and the integral extends over the DLA volume. From the models of Bakes & Tielens (1994) and Weingartner & Draine (2001), WPG03 find that  $\Gamma = 10^{-5} \kappa \epsilon J_\nu(\mathbf{r})$  where  $\kappa$  is the dust-to-gas ratio,  $\epsilon$  is the heating efficiency, and  $J_\nu(\mathbf{r})$  is the FUV mean intensity. Assuming DLAs are uniform disks with radius  $R$  and scale-heights  $h$ , and adopting the solution for  $J_\nu$  (WPG03) one finds

$$\mathcal{H} = 10^{-5} \frac{\kappa \epsilon \langle N \rangle}{8\pi} [1 + \ln(R/h)] \int \phi(L_\nu) L_\nu dL_\nu \quad , \quad (12)$$

where  $\langle N \rangle$  is the average H I column density of the DLA sample. Because  $\dot{\rho}_* = 1.25 \times 10^{-28} \int \phi(L_\nu) L_\nu dL_\nu$  (Madau et al. 1998), the comoving heating rate  $\mathcal{H}$  is proportional to  $\dot{\rho}_*$ . Assuming parameters adopted by Wolfe et al. (2004), we find that our upper limit on  $\dot{\rho}_*$  implies  $\mathcal{H} < 4 \times 10^{37} \text{ ergs s}^{-1} \text{ Mpc}^{-3}$ . Therefore, *in situ* star formation in DLAs is unlikely to account for the energy input needed to balance cooling.

Consequently the new limits on  $\dot{\rho}_*$  require an external source of metals and heat input for DLAs with  $\ell_c > 10^{-27.1} \text{ ergs s}^{-1} \text{ H}^{-1}$ . This idea was first discussed by WGP03 who suggested that centrally located galaxy bulges could heat the absorbing gas. Wolfe (2005) then suggested LBGs as the most natural bulge sources. In this scenario the FUV radiation originates in the LBGs, is attenuated by their high dust content, and then propagates unattenuated throughout DLAs because of their low dust content. The LBGs heat the surrounding DLA gas, with the same FUV radiation observed by us to have  $\dot{\rho}_* = 10^{-1.7} \text{ M}_\odot \text{ yr}^{-1} \text{ Mpc}^{-3}$  at  $z=3$  (e.g. Giavalisco et al. 2004). From Eq. 12, which also applies for central point sources (WGP03), we find the resulting LBG heating rate to be  $\mathcal{H} = (3 \pm 2) \times 10^{38} \text{ erg s}^{-1} \text{ Mpc}^{-3}$ , where the large systematic errors stem from uncertainties in the dust composition, photoelectric heating efficiency, geometry, etc. Nevertheless

this estimate suggests that embedded LBGs can explain the heating rate inferred for DLAs with  $\ell_c > 10^{-27.1}$  ergs s<sup>-1</sup> H<sup>-1</sup>.

The physical association of high- $z$  DLAs with LBGs is supported by the following phenomena. First, Cooke et al. (2006) recently measured the 3-D cross correlation function between DLAs and LBGs and found good agreement between the DLA-LBG cross-correlation amplitude and the LBG-LBG autocorrelation amplitude. This implies a similarity in the dark-matter masses of the two populations; i.e., a strong overlap between DLAs and LBGs. Further evidence for this association comes from the identification of at least one high- $z$  DLA with an LBG (Møller et al. 2002). In this object the FUV surface-brightness of the compact emitting regions is two orders of magnitude higher than predicted by the Kennicutt-Schmidt law applied to the H I column-density detected in absorption. This suggests that star formation originates in compact, presumably dusty, regions rarely detected in absorption, which are surrounded by the lower column-density gas that gives rise to the DLA. This configuration brings to mind the “tadpole galaxies” discussed in § 3.2 and indicates that their star forming regions may also be embedded in DLA gas. The low area covering factor and high column density implies that star formation in DLAs occurs in dense molecular regions (see Zwaan & Prochaska 2006), which are replenished with gas from the surrounding DLA. By contrast, the DLA gas may be chemically enriched by P-cygni winds emanating from the star-forming LBGs (Steidel et al. 2003). Other sources of metals may be pre-enriched gas or stars accreted by the galaxy hosting the DLA. The latter processes may be crucial for DLAs with  $\ell_c < 10^{-27.1}$  erg s<sup>-1</sup> H<sup>-1</sup>, which may not contain centrally located LBGs.

## 6. SUMMARY and CONCLUDING REMARKS

We searched for *in situ* star formation in the neutral gas comprising DLAs by looking for low surface-brightness emission from spatially extended objects in the Hubble Ultra Deep Field F606W image. The search was designed to detect objects in the redshift interval  $z = [2.5, 3.5]$  with linear *diameters* ranging between 1.9 kpc and 31 kpc, which encompasses most model predictions published so far. The search was optimized using a smoothing kernel to match the predicted size of the DLAs, ranging between an angular diameter of  $\theta_{\text{dla}} = 0.25''$  and  $4.0''$ . The results are summarized as follows:

- After eliminating compact objects with high surface brightness, we found the number of extended sources to decrease rapidly with increasing  $\theta_{\text{kern}}$ : the implication is that extended sources of low surface-brightness emission rarely occur in the UDF (see Fig. 3). Because photometric redshifts are unavailable, these findings lead to upper limits on the comoving density of objects within the UDF with  $z=[2.5,3.5]$ .

- The upper limits on comoving density lead to upper limits on comoving SFR density, which are between factors of 30 to 100 lower than predicted by the Kennicutt-Schmidt law. As a result, the projected SFRs per unit area must be at least a factor 10 lower than the rates predicted by the

distribution of neutral-gas column densities in DLAs. The upper limits are quite general as they apply to objects with angular diameters encompassing the sizes of DLAs in  $\Lambda$ CDM and all other models suggested so far.

- We suggest that lower SFR efficiencies may partly result from an increase with redshift of the critical surface density for Toomre instability. Such an increase is due to cosmological evolution alone. This effect causes the DLA gas to be Toomre stable, which could remove the discrepancy between the comoving SFR density predicted by the Kennicutt-Schmidt law and our empirical upper limits. However, the uncertainties are such that gravitational instabilities may be present in DLAs. In that case we suggest that the low molecular content of the gravitationally bound clouds with  $N < 10^{22} \text{ cm}^{-2}$  prevents further cooling and thus inhibits star formation. The low molecular content of the gas may be related to the minimum column density required for molecule formation (Krumholz & McKee 2005; Blitz & Rosolowsky 2006) since molecule formation in objects with low dust content and high FUV radiation fields such as found in DLAs could require values of  $N$  exceeding  $10^{22} \text{ cm}^{-2}$  for shielding against photo-dissociating radiation. The low area covering factor of such high column densities may be the reason for the low molecular content measured in DLAs.

- The upper limits on comoving SFR density reduce the rate of metal production predicted in DLAs. The resultant upper limits on metallicity at  $z \sim 3$  are lower than the observed metallicities by a factor of three. While this removes the previous problem of metal overproduction (by a factor of ten) in DLAs, it leads to a new problem of metal underproduction.

- The upper limits on comoving SFR density result in a comoving grain photoelectric heating rate that is significantly lower than the comoving cooling rate inferred from [C II]  $158 \mu\text{m}$  emission rates for about half the DLA sample. Therefore, external sources of heating are required. We argue that the observed comoving SFRs of LBGs with  $R < 27$  and  $z=[2.5,3.5]$  indicate a heat input sufficient to balance cooling.

- We suggest a scenario in which half the DLA population with significant [C II]  $158 \mu\text{m}$  cooling is powered by centrally located, compact LBGs. We speculate that DLA metal enrichment may be due to P-cygni outflow from the metal-enriched LBGs. The half of the DLA population without significant [C II]  $158 \mu\text{m}$  cooling is presumably heated by background radiation alone. Without an LBG, the source of metals for this DLA population is unclear.

Two possible caveats come to mind. First, since our limits do not apply to emission from DLAs with  $\theta_{\text{dla}} < 0.25''$ , it is possible that for most DLAs at  $z \sim 3$ ,  $d_{\text{dla}}$  is less than 1.9 kpc and the SFRs follow the Kennicutt-Schmidt relation. However, as discussed in § 3.1 all models suggested so far predict that the bulk of DLAs will have diameters larger than 1.9 kpc.

The second caveat stems from the possibility that *in situ* star formation at the Kennicutt-Schmidt rate occurs in DLA gas associated with high surface-brightness objects, since such objects were automatically excluded from the survey. We tested this hypothesis by searching for low surface-brightness emission surrounding high surface-brightness objects. To enhance the sensitivity

of our search we smoothed the regions in the F606W image surrounding selected targets using kernels with  $0.5'' < \theta_{\text{kern}} < 2.0''$ . In all cases the convolved images failed to show evidence for outlying emission with fluxes comparable to the central object. But it is difficult to draw conclusions from these data since the redshifts of all but two galaxies, at  $z = 2.593$  (Szokoly et al. 2004) and  $z = 3.797$  (Vanzella et al. 2006), respectively, are unknown. We found these two galaxies to consist of a compact core (FWHM =  $0.3''$ ) surrounded by diffusion emission, which exhibited maximum contrast with respect to sky when  $\theta_{\text{kern}} = 0.5''$ . In the case of the  $z=2.593$  galaxy the magnitude of the diffuse emission,  $V=30$ , while the central core has  $V = 25$ ; i.e., the regions surrounding this star-forming galaxy contributes less than 1 % of the total SFR. Because  $\rho_*$  due to compact star forming galaxies is comparable to  $\dot{\rho}_*$  predicted by the Kennicutt-Schmidt relation for DLAs, we would conclude that neutral gas surrounding star-forming objects does not form stars according to the Kennicutt-Schmidt relation if this galaxy is typical of its class.

Finally we compare our empirical limits with previous analyses that apply the local Kennicutt-Schmidt law for evaluating  $\rho_*$  in DLAs. First, Lanzetta et al. (2002) measured the frequency distribution of projected SFR per unit area,  $h(\dot{\psi}_*)$ , for galaxies in the HDF in the redshift interval  $z=[0,10]$ . Their measurements at  $z \sim 3$  were sensitive to  $\dot{\psi}_* \geq 10^{-1.5} \text{ M}_\odot \text{ yr}^{-1} \text{ kpc}^{-2}$ . To determine  $h(\dot{\psi}_*)$  at lower values of  $\dot{\psi}_*$ , they applied the Kennicutt-Schmidt law to the H I column-density distribution function  $f(N, X)$  by using the relation  $h(\dot{\psi}_*)d\dot{\psi}_*=(H_0/c)f(N, X)dN$ . They then used Eq. 6 in the spherically symmetric limit to determine  $\rho_*$ . These authors concluded that at  $z \approx 3$  the bulk of SFR density resides in regions of  $0.1 \text{ M}_\odot \text{ yr}^{-1} \text{ kpc}^{-2}$ , where the majority of LBG's are found. They argued that DLAs of  $N < 5 \times 10^{21} \text{ cm}^{-2}$  contribute an insignificant fraction of the global SFR density. This is inconsistent with the current form of  $f(N, X)$  which when extrapolated to  $N \gg 2 \times 10^{22} \text{ cm}^{-2}$ , to include HSB objects such as LBGs, predicts that more than 50 % of  $\rho_*$  is contributed by DLAs with  $N < 5 \times 10^{21} \text{ cm}^{-2}$ , even when  $K=K_{Kenn}/2.8$  as suggested by Lanzetta et al. (2002). The discrepancy stems from the different expressions used to compute  $f(N, X)$ : Lanzetta et al. (2002) used the then available expression for  $f(N, X)$  with slope,  $\alpha_3=-1.4$ , that is flatter than  $\alpha_3=-2.0$  derived for the more accurate SDSS function (PHW05) used here. Because we have shown that the DLA contribution to  $\rho_*$  cannot be this large, the newer data do not support the suggestion of Lanzetta et al. (2002) that SFRs predicted by application of the Kennicutt-Schmidt law to DLAs overlap those derived directly from optical emission. On the other hand, their analysis is consistent with our interpretation that LBGs provide the bulk of the star formation at  $z \sim 3$ . Second, Hopkins et al. (2005) combined an updated version of  $f(N, X)$  with the Kennicutt-Schmidt relation to predict  $\rho_*$  in the spherically symmetric limit for the redshift interval  $z=[2.5,3.5]$ . These authors concluded that DLAs contribute roughly 50% of the observed SFR density at  $z \sim 3$ . Again, the predicted  $\rho_*$  is significantly higher than our empirical upper limits, and thus their models are ruled out by the UDF data. The new upper limits on  $\rho_*$  are also inconsistent with the predictions of the uniform-disk model of WPG03 and WGP03. Their models do not make use of the Kennicutt-Schmidt law, but rather use the strength of C II\* absorption to infer the level of *in situ* star formation throughout DLAs modeled as uniform disks. Because the predicted average projected SFR,  $\langle \dot{\psi}_* \rangle = 10^{-2} \text{ M}_\odot \text{ yr}^{-1} \text{ kpc}^{-2}$ , is above our detection threshold,

the factor of 100 disagreement between the predicted  $\rho_*$  and our upper limits rules out this model. On the other hand, the new upper limits are consistent with the “bulge model” suggested by WGP03. In this model, star formation does not occur in the gas detected in absorption, but rather arises in a centrally located compact region, which heats the surrounding disk gas by emitting FUV radiation. The rough agreement between the comoving heating rate supplied by LBGs and the comoving cooling rate of DLAs suggests the bulges are in fact LBGs.

We wish to thank Eric Gawiser, Kim Griest, Andrei Kravtsov, and Jason X. Prochaska for valuable discussions. AMW was partially supported by NSF grant AST 03-07824 and H-WC was partially supported by NASA grant NNG06GC36G.

## REFERENCES

- Adelberger, K. L., & Steidel, C. C., 2000, *ApJ*, 544, 218
- Bahcall, J. N. & Peebles, P. J. E., 1969, *ApJ*, 156, L7
- Bakes, E. L. O., & Tielens, A. G. G. M. 1994, *ApJ*, 427, 822
- Bertin, E., & Arnouts, S. 1996, *A&AS*, 117, 39
- Blanton, M. R., Lupton, R. H., Schlegel, D. J., Strauss, M. J., Brinkmann, J., Fukugita, M., & Loveday, J., 2005, *ApJ*, 631, 208
- Blitz, L., & Rosolowsky, E. 2006, *astro-ph/0605035*
- Boisser, S., Peroux, C., & Pettini, M., 2003, *MNRAS*, 338, 131
- Bouwens, R. J., Illingworth, G. D., Blakeslee, J. P., Broadhurst, T. J., & Franx, M. 2004, *ApJ*, 611, L1
- Cen, R., Ostriker, J. P., Prochaska, J. X., & Wolfe, A. M. 2003, *ApJ*, 598 741
- Cooke, J., Wolfe, A. M., Gawiser, E., & Prochaska, J. X., 2006, *ApJ*, 636, 9L
- Elmegreen, B. G. 2002, *ApJ*, 577 206
- Fall, S. M., & Pei, Y. C., 1993, *ApJ*, 402 479
- Ferguson, A. M. N., Wyse, R. F. G., Gallagher, J. S., & Hunter, D. A. 1998, *ApJ*, 506 L19
- Gao, Y., & Solomon, P. M. 2004 *ApJS*, 152, 63
- Giavalisco, M., Dickinson, M., Ferguson, H. C., Ravindranath, S., Kretchmer, C., Moustakas, L. A., Madau, P., Fall, S. M., Gardner, J. P., Livio, M., Papovich, C., Renzini, A., Spinrad, H., Stern, D., & Riess, A. 2004, *ApJ*, 600, L103

- Gonzalez, A. H., Zaritsky, D., Dalcanton, J. J., & Nelson, A. 2001, *ApJS*, 137, 117
- Haehnelt, M. G., Steinmetz, M., & Rauch, M., 1998 *ApJ*, 495, 647
- Haehnelt, M. G., Steinmetz, M., & Rauch, M., 2000 *ApJ*, 534, 594
- Hopkins, A. M., Rao, S. M., & Turnshek, D. A., 2005 *ApJ*, 630, 108
- Howk, J. C., Wolfe, A. M., & Prochaska, J. X., 2005 *ApJ*, 662, L81
- Irwin, M. J. 1975, *MNRAS*214, 575
- Kauffmann, G. 1996, *MNRAS*, 281, 475
- Kennicutt, R. C., Jr. 1998a, *ARA&A*, 36, 189
- Kennicutt, R. C., Jr. 1998b, *ApJ*, 498, 541
- Kennicutt, R. C., Jr., Calzetti, D., Walter, F., Prescott, M. K., SINGS Team, 2005, *AAS*, 207, 6341
- Kravtsov, A., 2003, *ApJ*, 590, L1
- Krumholz, M. R. & McKee, C. F. 2005, *ApJ*, 630, 250
- Lanzetta, K. M., Noriaki, Y., Pascarella, S., Chen, H.-W., & Fernandez-Soto, A., 2002, *ApJ*, 570, 492
- Ledoux, C., Petitjean, P., & Srianand, R. *MNRAS*, 346, 209
- Madau, P., Pozzetti, L., & Dickinson, M. 1998, *ApJ*, 498, 106
- Martin, C. L., & Kennicutt, R. C. Jr. 2001, *ApJ*, 555, 492
- Metcalf, N., Shanks, T., Campos, A., McCracken, H. J. & Fong, R., 2001, *MNRAS*, 323, 795
- Mo, H. J., Mao, S., & White, S. D. M. 1998, *MNRAS*, 295, 319
- Møller, P., Warren, S. J., Fall, S. M., Fynbo, J. U., & Jakobsen, P. 2002, *ApJ*, 574, 51
- Nagamine, K., Springel, V., & Hernquist, H. 2004a, *MNRAS*, 350, 421
- Nagamine, K., Springel, V., & Hernquist, H.. 2004b, *MNRAS*, 350, 435
- Nagamine, K., Wolfe, A. M., Hernquist, L., & Springel, V. 2005, *astro-ph/0510729*
- Pei, Y. C., Fall, S. M., & Hauser, M. G. 1999, *ApJ*, 522, 604
- Pettini, M., 2004, *Cosmochemistry. The Melting Pot of the Elements*, ed. C. Esteban, A. Herero, R. Garcia-Lopez, F. Sanchez (Cambridge: Cambridge Univ. Press), 257

- Prochaska, J. X., & Wolfe, A. M. 1997, *ApJ*, 487, 73
- Prochaska, J. X., Gawiser, E., Wolfe, A. M., Castro, S., & Djorgovski, S. G. 2003, *ApJ*, 595, L9
- Prochaska, J. X., Herbert-Fort, S., & Wolfe, A. M. 2005, *ApJ*, 635, 123
- Razoumov, A. O., Norman, M. L., Prochaska, J. X., & Wolfe, A. M., 2005, [astro-ph/0510786](#)
- Schaye, J. *ApJ*, 609, 667
- Schmidt, M., 1959 *ApJ*, 129, 243
- Shapley, A. E., Steidel, C. C., Pettini, M., & Adelberger, K. L. 2003, *ApJ*, 588, 65
- Shu, F. H., Adams, F. C., & Lisano, Su. 1989, *ARA&A*, 25, 23
- Szokoly, G. P., Bergeron, J., et al. 2004 *ApJS*, 155, 271
- Spergel, D. N., Verde, L., Peiris, H. V., Komatsu, E., Nolta, M. R., Bennett, C. L., Halpern, M., Hinshaw, G., Jarosik, N., Kogut, A., Limon, M., Meyer, S. S., Page, L., Tucker, G. S., Weiland, J. L., Wollack, E., & Wright, E. L. *ApJS*, 148, 175
- Springel, V., & Hernquist, L. 2003, *MNRAS*, 312, 334
- Steidel, C. C., Adelberger, K. L., Giavalisco, M., Dickinson, M., & Pettini, M. 1999, *ApJ*, 519, 1
- Steidel, C. C., Adelberger, K. L., Shapley, A. E., Pettini, M., Dickinson, M., & Giavalisco, M. 2003, *ApJ*, 592, 728
- Straughn, A. N., Cohen, S. H., Ryan, R. E., Hathi, N. P., Windhorst, R. A., & Jansen, R. A. 2006, *ApJ*, 639, 724
- Toomre, A. 1964, *ApJ*, 139, 1217
- Tumlinson, J., Shull, J. M., Rachford, B. L., Browning, M. K., Snow, T. P., Fullerton, A. W., Jenkins, E. B., Savage, B. D., Crowther, P. A., Moos, H. W., Sembach, K. R., Sonneborn, G., & York, D. G. Windhorst, R. A., & Jansen, R. A. 2002, *ApJ*, 566, 857
- van Zee, L., Haynes, M. P., Salzer, J. J., & Broeils, A. H., 1997, *AJ*, 113, 1618
- Vanzella, F. et al. 2006, [astro-ph/0601367](#)
- Weingartner, J. C., & Draine, B. T., 2001 *ApJ*, 553, 581
- Wolfe, A. M., Lanzetta, K. M., Foltz, C. B., & Chaffee, F. H. 1995, *ApJ*, 454, 698
- Wolfe, A. M., Gawiser, E., & Prochaska, J. X. 2003a, *ApJ*, 593, 235 (WGP03)
- Wolfe, A. M., Prochaska, J. X., & Gawiser, E. 2003b, *ApJ*, 593, 215 (WPG03)

- Wolfe, A. M., Howk, J. C., Gawiser, E., Prochaska, J. X., & Lopez, S. 2004, *ApJ*, 615, 625
- Wolfe, A. M., Gawiser, E., & Prochaska, J. X. 2005, *ARA&A*, 43, 861
- Wolfe, A. M., 2005, in *Probing Galaxies through Quasar Absorption Lines*, Proceeding IAU Colloquium No. 199, eds. P. R. Williams, C. Shu, & B. Menard, (Cambridge: University Press), 148
- Wong, T., & Blitz, L. 2002, *ApJ*, 569, 157
- Yan, H., Dickinson, M., Eisenhardt, P. R. M., Ferguson, H. C., Grogin, N. A., Paolillo, M., Chary, R.-R., Casertano, S., Stern, D., Reach, W. T., Moustakas, L. A., & Fall, S. M., 2004, *ApJ*, 616, 63
- Zwaan, M. A., van der Hulst, J. M., Briggs, F. H., Verheijen, M. A. W., & Ryan-Weber, E. V. 2005, *MNRAS*, 364, 1467
- Zwaan, M. A., & Prochaska, J. X. 2006, *ApJ*, 643, 675